Elastic Properties and Line Tension of Self-Assembled Bilayer Membranes

ELASTIC PROPERTIES AND LINE TENSION OF SELF-ASSEMBLED BILAYER MEMBRANES

BY

KYLE PASTOR, B.Sc.

A THESIS

SUBMITTED TO THE DEPARTMENT OF PHYSICS & ASTRONOMY

AND THE SCHOOL OF GRADUATE STUDIES

OF MCMASTER UNIVERSITY

IN PARTIAL FULFILMENT OF THE REQUIREMENTS

FOR THE DEGREE OF

MASTER OF SCIENCE

Master of Science (2013) McMaster University

(Physics & Astronomy) Hamilton, Ontario, Canada

TITLE:	Elastic Properties and Line Tension of Self-Assembled Bilayer Membranes
AUTHOR:	Kyle Pastor B.Sc., (Physics & Astronomy) McMaster University, Hamilton, Canada
SUPERVISOR:	Dr. An-Chang Shi
NUMBER OF PAGES:	xii, 74

For Eddard Stark. Don't hate the player. Hate the game... of thrones... Except Joffrey. Everyone hates him.

Abstract

The bending moduli and line tension of bilayer membranes self-assembled from diblock copolymers was calculated using the self-consistent field theory. The limitation of the linear elasticity theory (Helfrich model) was evaluated by calculating fourth-order curvature moduli in high curvature systems. It was found that in highly curved membranes, the fourth-order contributions to the bending energy becomes comparable to the low-order terms. The line tension (γ_L) of membrane pores was also investigated for mixtures of structurally different diblock copolymers. The line tension was found to depend sensitively on the diblock chain topology. Addition of short hydrophobic copolymers was found to reduce the line tensions to negative values, showing that lipid mixtures may be used as pore stabilizers.

Acknowledgements

Whenever I read an acknowledgements section they are always so heart-felt and mushy. However, this is my section so lets have some fun with it. Of course there are people that I want to thank, like my parents Joe and Miriam Pastor, and my brother Nick and sister Michelle. Aunts, uncles, cousins, grandmas and grandpas, and Eggo, my bunny. Even my dead hamster Cheerio. RIP 2008-2010. Also especially my wonderful girlfriend Laura. I want to also thank my supervisor An-Chang Shi for keeping me on track and providing a challenging but rewarding experience. To my committee members, sorry you have to read the many pages of my ramblings and likely copious amounts of spelling erors. I want to also say thanks to Ash Dehghan for collaborating on the pore systems, and also for all the good times since first year in Woodstock. Lastly, I have but one request to Ash. Please follow this link: http://bit.ly/N4sQIX. Game Over friend.

Contents

Abstract **iv**

Acknowledgements **v**

1 Introduction **1**

2 Model and Methods **8**

2.1 Self-Consistent Field Theory (SCFT) 9

2.2 Excess Free Energy of the Bilayer Membrane 10

2.3 Geometric Considerations 13

3 Single-Component Bilayers **17**

3.1 Second-Order Moduli (κ_M, κ_G) 20

3.2 Fourth-Order Moduli (B_C, B_S) 29

3.3 Limitation of the Helfrich Free Energy 35

4 Two-Component Bilayers **38**

4.1 Hydrophobic Mismatched Lipids 39

5 Line Tension of Bilayer Membrane Pores **43**

6 Summary **52**

A Numerical Methods **56**

A.1 Crank-Nicolson Method 57

A.1.1 Planar Coordinate System 57

A.1.2 Cylindrical Coordinate System 59

A.1.3 Spherical Coordinate System 60

A.1.4 Crank-Nicolson Boundary Conditions 61

A.2 Alternating Direction Implicit Method (ADI) In Cylindrical Coordinates 65

List of Figures

1.1 Various morphologies of self-assembled lipid molecules in solvent. Depending on properties such as lipid concentration, bending rigidities and solvability, different configurations are stable (Original image by Mariana Ruiz Villarreal). 2

3.1 A typical concentration profile for a curved bilayer membrane. The hydrophobic tail regions (ϕ_B) are shielded from the solvent (ϕ_C) by the hydrophilic head groups (ϕ_A). The average thickness of the bilayer is typically $d = 4.3R_g$, which is used as the curvature length scale in the system. The vertical (red) line shows the maxima of the hydrophobic concentration, used to define the bilayer neutral plane. 18

3.2 Diagram showing the radius of a cylindrical geometry to the inner edge of the computation cell (shown in red). This distance r_0 can be adjusted to allow for a wide variety of curvatures without the need to change the computation cell. 19

3.3 Free energy as a function of the scaled curvature for the cylindrical (F^C) and spherical (F^S) geometries. At $cd = 0$ the bilayer is essentially flat, regardless of the geometry, and attains the planar value of zero energy. For cases of low curvature $cd \approx 0.0 - 0.5$, there is a quadratic relationship between the curvature and free energy. In systems of high curvature $cd > 0.5$, fourth-order terms enter the free energy and deviations away from the linear Helfrich model occur. . . 20

3.4 Bending modulus (κ_M) for chain fractions of $f_A = 0.3 - 0.7$, for interactions of $\chi_{AB}N = \chi_{BC}N = 25, 30, 35$. The results show that the chain fraction does not have a dramatic effect on κ_M, while an increase in interaction strength reinforces the mechanical strength of the bilayer. 21

3.5 Gaussian modulus (κ_G) for chain fractions of $f_A = 0.3 - 0.7$, for interactions of $\chi_{AB}N = \chi_{BC}N = 25, 30, 35$. A transition from positive modulus values to negative occurs at $f_A \approx 0.4$, which signifies a change in the preferred topology. 23

3.6 Ratio of the Gaussian modulus κ_G relative to the bending modulus κ_M. Biological membranes have been shown to take on a value close to $\kappa_G/\kappa_M = -1$. This result can be used to compare the simplified model presented with biological membrane systems. 25

3.7 Bending modulus (κ_M) as a function of the hydrophilic chain fraction f_A for different solvent interaction values. Increasing $\chi_{AC}N$ causes a decrease in the rigidity of the chain. 26

3.8 Gaussian bending modulus (κ_G) as a function of the hydrophilic chain fraction f_A for different solvent interaction values. Small changes in the solvent chemistry leads to an upwards shift in κ_G. For $\chi_{AC}N > 3$, the Gaussian modulus is strictly positive which may promote non-spherical topologies. 28

3.9 Bending modulus (κ_M) for a variety of homopolymer length fractions κ. When the homopolymer is longer than the AB diblock it is unable to hydrate the hydrophilic head groups leading to a decrease in the bending rigidity. The solvent also has an effect on the position of the maximal bending rigidity, leading to a more pronounced asymmetry. . 30

3.10 Gaussian bending modulus (κ_G) for different homopolymer length fractions κ. An increase in the homopolymer length shifts κ_G to more positive values and shifts the zero crossing transition. 31

3.11 Fourth-order cylindrical bending modulus (B_C) for the AB/A system. Positive values are found for B_C which are expected since B_C is simply a high-order mean curvature scaling factor. A negative linear trend with f_A is also observed. 33

3.12 Fourth-order spherical bending modulus (B_S) for the AB/A system. The negative values show that the combination of the bending moduli cause a lowering of the free energy at high curvatures. It should be noted that B_S contains the coupling term κ_2 between the mean curvature M and the Gaussian curvature G. 34

3.13 Critical curvature phase diagram for the hydrophilic chain fractions (f_A) and scaled curvature (cd). The filled regions show the parameter space where the bending energy is accurately described by the standard Helfrich description. In the unfilled fourth-order region, the high-order moduli must be added to describe the energetics of bending the bilayer membrane. 37

4.1 Diagram depicting the various conical shapes taken by the CD diblock copolymer. Smaller tail fractions (f_D), shown as hashed (blue) segments, give the diblock a more conical geometry. 40

4.2 The effect of the mixing of short tail (CD) diblocks into a symmetric diblock (AB) bilayer, on the bending rigidity (κ_M) of the membrane. The result is shown for a variety of chain lengths (f_D). The values of $\Psi = 1$ correspond to pure symmetric diblock (AB), and $\Psi = -1$ are pure short tail (CD) dibocks. 41

5.1 Schematic of pore formation in the cylindrical geometry. The radius from the centre of the geometry to the innermost edge of the computation cell is shown. Varying r_0 allows for pores of different sizes to be created, and their free energy calculated. Also shown is the typical concentration profile of the membrane pore, where the computation cell is the (red) box surrounding the profile. 44

5.2 Free energy of the membrane pore as a function of pore radius (r/d). Depending on the length of the secondary diblock in the bilayer, the free energy can take shallower slopes. The linear relationship is used to extract the edge line tensions γ_L. 45

5.3 Scaled line tension ($\tilde{\gamma}_L$) as a function of the hydrophilic chain fraction (f_A). The line tension is a monotonically decreasing function with chain fraction and has a zero transition at $f_A \approx 0.6$. Negative line tensions can lead to stable pore formation in the bilayer membrane. . 46

5.4 Edge line tension ($\tilde{\gamma}_L$) as a function of relative diblock concentration (Ψ) for a variety of secondary diblock geometries. More conical shaped diblock correspond to smaller hydrophobic tail segments (f_D). The addition of conical diblocks reduces the line tension of the pore. For very short tailed diblocks ($f_D < 0.3$), mixtures can lead to negative line tensions, making pore formation favourable. 47

5.5 Concentration profile of the secondary conical CD diblock forming a membrane pore. The diblocks at the edge are represented as cones. The $3D$ representation shows edge phase separation of the conical diblock (dark/blue). 49

5.6 Total concentration of each polymer species as a function of the radial direction. The increase in the CD concentration quantifies the amount of separation in the system. 50

Chapter 1

Introduction

The cell membrane is what separates the internal content of a biological cell from the external environment. In recent years, much attention has been focused on the role played by the cell membrane in cellular mechanisms such as fusion, protein integration and endo/exocytosis [1–5]. Cell membranes are mainly composed of amphiphilic lipid molecules which have hydrophilic head groups and hydrophobic tail groups, allowing for self-assembly when mixed with water [6,7]. This self-assembly can lead to a variety of morphologies such as spherical and cylindrical micelles as well as bilayer vesicles (liposomes), where two lipid monolayers oppose each other and encase the solvent inside its volume (Fig. 1.1). In real biological systems the lipid bilayer does not exist in isolation. The bilayer itself may contain a variety of different lipid molecules as well as cholesterol and a wide array of surface bound and transmembrane proteins [7, 8]. The environment in which the bilayer exists in is also highly diverse. For instance, ion concentration differences between the inside and outside of the membrane can lead to potential gradients, or action potentials [8]. Beyond this, there are differences in lipid composition between bilayer leaflets caused by both production rates of lipids

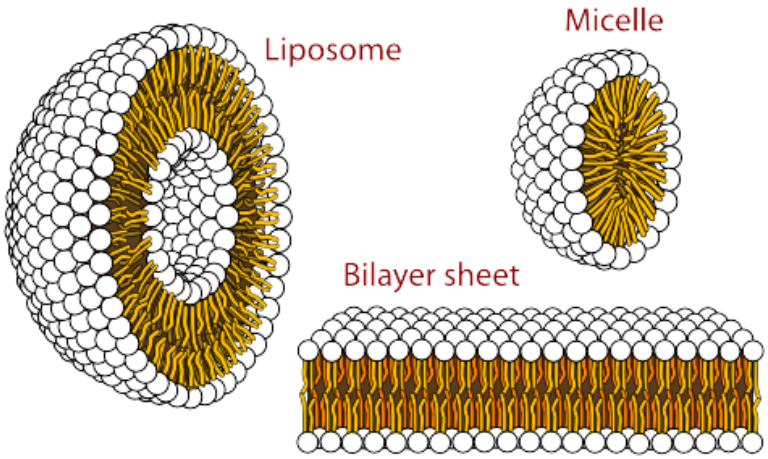

Figure 1.1: Various morphologies of self-assembled lipid molecules in solvent. Depending on properties such as lipid concentration, bending rigidities and solvability, different configurations are stable (Original image by Mariana Ruiz Villarreal).

within the cell (lipogenesis) and the relatively slow rate of inter-leaflet switching of lipids (flip-flop rate). All of these factors make the membrane a vastly complex and important structure. As such, much effort has gone into understanding the physics of these systems from a theoretical and experimental viewpoint.

Due to the extreme complexity of biological membranes, simplified models have been used to understand their basic properties. One such approximation is that of a pure lipid bilayer which contains no proteins and only a single type of lipids. In order to understand the physical characteristics of these systems research has been conducted utilizing experimental, computational and theoretical methods [9–15]. A fundamental understanding of the basic mechanical properties of these membranes is of great practical importance in drug development and delivery [5], understanding disease through knowledge of protein mediation [1, 2], lipid raft formation [16, 17] and a variety of other large scale cellular functions such as membrane budding [17],

fission/fusion [3,4] and endo/exocytosis [5]. Intra-cellular structures such as organelles are also composed of membranes. For example, the cell nucleus is surrounded by a porous double membrane known as the nuclear envelope. Other organelles such as the endoplasmic reticulum, the Golgi apparatus, and the mitochondria are all membrane bound systems [7, 18]. It is clear that from a biological perspective, understanding the basic properties of the bilayer membrane will lead to a large array of applications.

A commonly used method for modelling the bilayer is the continuum model which treats the lipid bilayer as a thin elastic sheet. This was first proposed by Canham [19] where the shape of red blood cells was determined by modelling the membrane with the beam equation. An expansion of this work was done by Helfrich [20], where he modelled the bilayer as a nematic liquid crystal, which was first studied by Frank [21]. The theory assumes no internal structure and simplifies the system to depend on just a few geometric parameters. Using the mathematics of differential geometry, the surface is described by its two principle curvatures, c_1 and c_2. Combinations of these principle curvatures are used to parameterize the surface, which are the mean curvature $M = (c_1 + c_2)/2$ and the Gaussian curvature $G = c_1 c_2$ [22]. Through the derivation performed by Canham and later Helfrich, the energy for curving a membrane away from its equilibrium can be represented as,

$$F = \int [2\kappa_M (M - c_0)^2 + \kappa_G G + \sigma_0] dA + \int \gamma_L dl \tag{1.1}$$

where κ_M, κ_G, σ_0 and γ_L are the bending modulus, the Gaussian bending modulus, the surface tension and the edge tension, respectively. Calculations of these bending moduli are useful for understand the mechanical properties of bilayer systems. A linear expansion of the curvature about the equilibrium (spontaneous) curvature c_0

is used to obtain Eq. 1.1. This model is known to be valid in cases of small curvature deformations, however there has been limited work regarding the validity of this model in highly curved systems. For example, Harmadaris *et al.* [9] tried to test this using a two bead approximation for the lipid tails and found that the linear elastic model was valid for curvatures up to the bilayer thickness. However, the two bead approximation limits the contributions from the lipid tails and calls into question the accuracy of the study. It has also been shown that fourth-order moduli can stabilize intermediate states in the disk-to-vesicle transition of bilayer membranes [23]. Accurate calculations are crucial in understanding what processes are biologically relevant. For example, a review by Nagle [24] outlines how within the current literature, the value of the experimentally measured bending modulus κ_M varies by a factor of two depending on the method used. Since the free energy is carried into the exponential when calculating the probability of certain biological processes, this disagreement between studies can be significant. It is this reason that the calculation of high-order curvature terms are important. Small changes in the calculated moduli and free energy can have a profound effect on the chances of seeing certain structures/processes in nature. For this reason, as well as its wide used in the literature [3–5, 10, 12, 13], an understanding of the limitations of the Helfrich model is important.

This thesis presents an investigation on the contribution of higher-order correction terms in the Helfrich free energy (Eq. 1.1), and outlines a systematic method for determining the bending moduli using the self-consistent field theory (SCFT). The expression used for the higher-order corrections, henceforth referred to as the modified

Helfrich free energy is given as,

$$F = \int [2\kappa_M M^2 + \kappa_G G + \kappa_1 M^4 + \kappa_2 M^2 G + \kappa_3 G^2 + \sigma_0] dA + \int \gamma_L dl \qquad (1.2)$$

where κ_1,κ_2 and κ_3 are the fourth-order bending moduli. In Eq. 1.2, it is assumed that the bilayers are symmetric, thus eliminating odd order terms as well as sets the spontaneous curvature to $c_0 = 0$. Recently a similar model has been used to investigate the energetics of bolaamphiphilic membrane systems [24–27]. These studies show that the high-order terms become important for the stability of various morphologies. Even though the systems studied in Refs. [24–27] are different from the one presented here, it shows that higher-order terms can be significant in some cases and serves as further motivation for the current work. To calculate the bending moduli, a theoretical description, the Self-Consistent Field Theory (SCFT), was used. The SCFT is a widely utilized statistical description of polymeric melts that allows for the computation of the free energy and detailed properties such as the morphology (concentration distributions) [28–30]. By modelling a lipid bilayer immersed in solvent as a blend of AB diblock copolymers (lipids) mixed with C homopolymers (solvents), a bilayer can be stabilized in a variety of geometries (planar, cylindrical, spherical). The free energy as a function of the bilayer curvature is then determined. By fitting the free energy as a function of curvature to the modified Helfrich expression (Eq. 1.2), the bending moduli are obtained. A critical curvature is calculated depending on the relative change in free energy between the standard and modified Helfrich models. This analysis is vital for understanding the bending energetics of systems that exhibit curvature on the order of the bilayer thickness, found in membrane fusion and fission, endo/exocytosis and membrane budding.

Armed with a systematic method for finding the bending moduli, a study on the effect of the molecular parameters, such as the hydrophilic chain fraction (f_A) and interaction parameters (χN), on the system was performed. Modification of solvent conditions and their effect on membrane properties was also analyzed. Solvents are known to play a role in certain cellular functions such as creating potential gradients across the membrane due to differential ion concentrations [8]. Understanding the effect of mixing lipids (diblocks) of different chemical types in a solvent (homopolymer) has been studied in the past [17], however a systematic description over an array of parameters has not been carefully investigated. Mixing of chemically different lipid types have been shown to induce large scale morphological changes in vesicles, and to promote budding transitions [31]. For this system, the bending modulus κ_M for a range of lipid compositions is studied for mixtures of lipids that have a hydrophobic mismatch between their tail sections.

Using the SCFT, the line tension of membrane pores was also calculated. The line tension γ_L present in Eqs. (1.1, 1.2) plays an important role in pore formation. Sakuma *et al.* [32] have shown that mixtures of lipids (diblocks) of different conical shapes (hydrophobic tail lengths) can lead to induced spontaneous curvatures through pore mediated inter-leaflet lipid transfer and reduced line tensions, allowing for stable pore formations as well as complex morphologies to occur. These conical lipids may therefore be used as edge stabilization agents in biological systems [33]. This report ends with a qualitative description of pore edge phase separation in two-component membrane systems and what effect it has on the edge line tension.

Through a deeper understanding of the effects that various system parameters play on the mechanical properties of bilayer membranes, it is hoped that the results

presented here can prove as a useful guide for future work. Having a more accurate understanding of the bending energetics of such systems can help experiments elucidate the mechanisms that drive cellular processes.

Chapter 2

Model and Methods

In this section, a description of the systematic methods used to determine the various bending moduli of the bilayer membrane is presented. Since the theoretical derivation of the Self-Consistent Field Theory (SCFT) is rather long and involved, only the main results are shown in this chapter. A more detailed description is found in standard texts [34]. In the following sections, a description of the SCFT is given and the excess free energy of a bilayer system is defined. The difference between the free energy of a flat bilayer, found by SCFT and the bulk free energy gives a measure of the surface tension σ_0 of the membrane. In the systems considered here, it is convenient to find a zero surface tension condition ($\sigma_0 = 0$) by careful adjustment of the relative chemical potentials between all components of the system. This eliminates the energy contribution from changing the membrane area and is also a condition satisfied in real biological membranes. The later section describes how different geometries can be used to simplify the Helfrich free energy (Eq. 1.2) and how this model compares to the free energies determined by the SCFT calculations.

2.1 Self-Consistent Field Theory (SCFT)

Much research has recently been focused on understanding the properties of the lipid bilayers, and these have taken the form of experiments [12,32,35,36], theory and simulations [2,9–11,15]. For an understanding of the physics of membrane deformations, as well as large scale shape transitions, for example endo/exocytosis, there is a need for large system scales as well as a very large number of particles. For these reasons, there is a large numerical cost associated with these methods, and constrains the effectiveness of some numerical calculations. Work has been done in the past using atomistic, coarse grained molecular dynamics (MD) and dissipative particle dynamics (DPD) to study the bilayer membrane [17, 37]. The major limitation that impacts these methods is the computational cost to simulate the many particles needed to accurately describe a bilayer membrane. Simulations exploring the bending moduli often have to measure the modes of bilayer shape fluctuations which can be fit with a power law [9, 38]. However, this method is limited to low curvature fluctuations due to small gradient expansions about the equilibrium shape [38]. The SCFT method used in this thesis is a statistical model, which replaces all interactions between the large number of polymers with an effective field acting on a single polymer chain. This eliminates the limitation of simulation size, and also allows for direct calculation of the system free energy, which has proved challenging in particle based simulations.

The SCFT starts with a microscopic representation of the polymer or polymer blend, which is composed of individual statistical segments of a certain size. A simple description of the polymer is given using the Gaussian chain model, which represents the polymer as a series of spherical segments connected by freely rotating springs [34, 39]. Using the Flory-Huggins description to model the chain interactions,

a grand canonical system is written, which is needed to describe the bilayer where the membrane must remain in a tensionless self-assembled state. A mean-field approximation is used to calculate the critical points of the free energy landscape with respect to the fields. This chooses a single dominant configuration that is assumed to be the only contributing state in the partition function [34]. With this, a set of self-consistent equations are found that can be solved numerically. These solutions are then used to calculate the free energy of the bilayer system.

2.2 Excess Free Energy of the Bilayer Membrane

The methods described here can be applied to a variety of model systems with little modification to the theory. The simplest system studied is a mixture of AB diblock copolymers, which model the lipids of the biological membrane and C homopolymers acting as the solvent. The SCFT calculation gives the free energy density of a grand canonical ensemble for this system to be,

$$\begin{aligned}
\frac{N\mathcal{F}_{SCFT}}{R_g^3\rho_0 V} &= \frac{1}{2V}\sum_{\alpha\neq\alpha'} N\chi_{\alpha\alpha'}\int d\vec{r}\phi_\alpha(\vec{r})\phi_{\alpha'}(\vec{r}) - \frac{1}{V}\sum_{\alpha}\int d\vec{r}\omega_\alpha(\vec{r})\phi_\alpha(\vec{r}) \\
&+ \frac{1}{V}\int d\vec{r}N\eta(\vec{r})(\sum_{\alpha}\phi_\alpha(\vec{r}) - 1) \\
&+ \frac{1}{V}\int d\vec{r}N\xi(\vec{r})\delta(\vec{r}-\mathcal{R})(\phi_A(\vec{r}) + \phi_C(\vec{r}) - \phi_B(\vec{r})) \\
&- e^{\Delta\mu_1}Q_1 - e^{\kappa\Delta\mu_2}\frac{Q_2}{\kappa}
\end{aligned} \tag{2.1}$$

where ρ_0 is the segment density, N is the degree of polymerization of the AB diblock, $R_g = \sqrt{N/6}b$ is the radius of gyration of the AB diblock, $\Delta\mu_p$ are the chemical

potentials of each polymer type ($p = 1$ for diblock, $p = 2$ for homopolymer), κ is the relative homopolymer length and Q_p are the single chain partition functions. $\phi_\alpha(\vec{r})$ and $\omega_\alpha(\vec{r})$ are the concentration and auxiliary fields of the $\alpha = A, B, C$ type polymer. Here, $\eta(\vec{r})$ and $\xi(\vec{r})$ are the incompressibility and the pinning conditions, respectively. As described in detail in Ref. [33], the $\xi(\vec{r})$ constraint field is needed to stabilize the bilayer for the various geometries.

In order to calculate Eq. 2.1, the various fields $(\phi, \omega, \eta, \xi)$ and single chain partition functions (Q_p) must be found. The single chain partition functions are calculated as,

$$Q_1(\{\omega_\alpha\}) = \frac{1}{V}\int d\vec{r}_1 d\vec{r}_2 d\vec{r}_3 Q_A(\vec{r}_1, N_A|\vec{r}_2, 0) Q_B(\vec{r}_2, N_B|\vec{r}_3, 0) \tag{2.2a}$$

$$Q_2(\{\omega_\alpha\}) = \frac{1}{V}\int d\vec{r}_1 d\vec{r}_2 Q_C(\vec{r}_1, N_C|\vec{r}_2, 0) \tag{2.2b}$$

where $Q(\vec{r}, s|\vec{r}', 0)$ are the chain propagators that take the form,

$$Q(\vec{r}, s|\vec{r}', 0) = \int_{\vec{R}(0)=\vec{r}'}^{\vec{R}(s)=\vec{r}} \mathcal{D}[\vec{R}(s)] e^{-\int_0^N ds \left(\frac{3}{2b^2}\left[\frac{d\vec{R}(s)}{ds}\right]^2 + \omega(\vec{R}(s))\right)} \tag{2.3}$$

The chain propagators are found by solving a modified diffusion equation,

$$\frac{\partial}{\partial s} Q_\alpha(\vec{r}, s|\vec{r}') = \frac{b^2}{6}\nabla^2 Q_\alpha(\vec{r}, s|\vec{r}') - \omega_\alpha(\vec{r}) Q_\alpha(\vec{r}, s|\vec{r}') \tag{2.4}$$

with an initial condition of $Q_\alpha(\vec{r}, 0|\vec{r}') = \delta(\vec{r} - \vec{r}')$. These can also be used to define

the end-integrated propagators,

$$q_\alpha(\vec{r},s) = \int d\vec{r}' Q_\alpha(\vec{r},s|\vec{r}') \tag{2.5}$$

$$q^+_\alpha(\vec{r},s) = \int d\vec{r}' d\vec{r}'' Q_\alpha(\vec{r},s|\vec{r}') Q_\beta(\vec{r}',N_\beta|\vec{r}'') \tag{2.6}$$

which satisfy the same modified diffusion equation. These are then used to calculate the fields of the system through a set of self-consistent field equations,

$$\phi_\alpha(\vec{r}) = e^{\Delta\mu_1}\int_0^{f_\alpha} ds q_\alpha(\vec{r},s) q^+_\alpha(\vec{r},f_\alpha - s) \quad \alpha = A,B \tag{2.7a}$$

$$\phi_C(\vec{r}) = \frac{e^{\kappa\Delta\mu_2}}{\kappa}\int_0^{\kappa} ds q_C(\vec{r},s) q^+_C(\vec{r},\kappa - s) \tag{2.7b}$$

$$\omega_\alpha(\vec{r}) = \sum_{\alpha\neq\beta}\chi_{\alpha\beta}N\phi_\beta(\vec{r}) + \eta(\vec{r}) + \xi(\vec{r}) \quad \alpha = A,C \tag{2.7c}$$

$$\omega_B(\vec{r}) = \sum_{B\neq\beta}\chi_{B\beta}N\phi_\beta(\vec{r}) + \eta(\vec{r}) - \xi(\vec{r}) \tag{2.7d}$$

$$\sum_\alpha \phi_\alpha(\vec{r}) = 1 \tag{2.7e}$$

$$\phi_A(\mathcal{R}) + \phi_C(\mathcal{R}) = \phi_B(\mathcal{R}) \tag{2.7f}$$

The free energy is found by solving the self-consistent field equations via commonly used numerical methods [40]. The solutions are then substituted into Eq. 2.1 to find the free energy. For comparison, the homogeneous (bulk) free energy density for the same system was used. In the case of homogenous systems, the spatial dependence of the fields is no longer present and the field variables become scalar. The self-consistent equations can be solved analytically to determine the homogenous polymer concentrations and free energy of the homogenous phase. With the spatial dependence

eliminated the free energy becomes,

$$\frac{N\mathcal{F}_{bulk}}{R_g^3\rho_0} = \frac{1}{2}\sum_{\alpha\neq\beta}\chi_{\alpha\beta}N\phi_\alpha\phi_\beta - \sum_\alpha \omega_\alpha\phi_\alpha - e^{\Delta\mu_1}Q_1 - e^{\kappa\Delta\mu_2}\frac{Q_2}{\kappa} \tag{2.8}$$

The excess free energy difference per unit area between the equilibrium SCFT solutions ($\mathcal{F}_{SCFT}$) and the bulk free energy ($\mathcal{F}_{bulk}$) is,

$$F = \frac{N(\mathcal{F}_{SCFT} - \mathcal{F}_{bulk})}{R_g^3 k_B T \rho_0 A} \tag{2.9}$$

where A is the area of the bilayer membrane, k_B is the Boltzmann constant and T is the temperature.

2.3 Geometric Considerations

As mentioned in the introduction, the overall goal is to create a systematic method to determine the various bending moduli in the system. Ideally, each of the bending moduli in Eq. 1.2 should be determined independently, however the calculations in this study are limited to a small number of geometries that can be used to measure the bending moduli, which are the planar (P), cylindrical (C), spherical (S) and in later applications the pore geometry ($Pore$). For each geometry, a different form of the modified Helfrich free energy (Eq. 1.2) is found. In this model there are seven coefficients and only four geometries, therefore the system of equations is underdetermined and it becomes impossible to extract all moduli independently. Some of these coefficients can be neglected by using assumptions and physical reasoning. The first

modification that can be done is to assume a closed, tensionless membrane ($\sigma_0 = 0$, $dl = 0$). The zero surface tension condition is found by careful adjustment of the chemical potentials ($\Delta\mu$) between the components of the system. First, a bilayer in a planar geometry is stabilized, giving a reference state which lacks any curvature terms ($M = G = 0$). This reduces Eq. 1.2 to,

$$F^P = \int \sigma_0 dA \tag{2.10}$$

where the superscript P denotes the planar geometry. Since the bilayer has a finite area, this means that if the condition $F^P = 0$ is found then the surface tension term σ_0 must be zero. Eq. 2.9 requires that $\mathcal{F}_{SCFT} = \mathcal{F}_{Bulk}$ for this condition to be true. This is easily determined using any root finding method, such as the secant method, to determine the correct chemical potentials that satisfy the condition. Once this condition is met, Eq. 1.2 can be written for a cylindrical geometry where the principle curvatures are $c_1 \equiv C = 1/R$, $c_2 = 0$ and R is the radius of the cylinder. The mean curvature becomes $M = C/2$ and the Gaussian curvature $G = 0$. After substituting these parameters into the free energy, the free energy calculated for the cylindrical geometry yields,

$$F^C = \frac{\kappa_M}{2} C^2 + B_C C^4 \tag{2.11}$$

In Eq. 2.11, the fourth-order curvature terms have been combined into a single term called the cylindrical fourth-order bending modulus $B_c = \kappa_1/16$. In the spherical case the principle curvatures are $c_1 = c_2 \equiv C$, and $M = C$, $G = C^2$, leading to a free energy,

$$F_S = (2\kappa_M + \kappa_G)C^2 + B_S C^4 \tag{2.12}$$

where the spherical fourth-order modulus is defined as $B_S = \kappa_1 + \kappa_2 + \kappa_3$. Finding the solutions at low curvatures give a quadratic response in the free energies which can be fit to a quadratic polynomial to extract κ_M and κ_G independently. To determine the fourth-order moduli, bilayers of high curvatures are used, which show an additional fourth-order response in the free energy. These are fit to a fourth-order polynomial to extract B_C and B_S.

Up to this point there has not been a definition of the length and energy scales of the system. To define the length scale, a tensionless planar bilayer is used as a reference state. The thickness of the planar bilayer for symmetric diblocks ($f_A = f_B = 0.5$); which was found to be $d = 4.3R_g$, was used as the length scale for the system curvatures. The energy scale is defined as the interfacial energy between two chemically distinct homopolymers of type A and B (diblock components). The strong segregation limit of such an interface is given as $\gamma_{int} = \sqrt{\chi N/6}(k_b T b \rho_0)/\sqrt{N}$ [41]. The bending moduli of the system are now rescaled as,

$$\tilde{\kappa}_M = \frac{\kappa_M}{\gamma_{int} d^2} \tag{2.13a}$$

$$\tilde{\kappa}_G = \frac{\kappa_G}{\gamma_{int} d^2} \tag{2.13b}$$

$$\tilde{B}_C = \frac{\kappa_1}{16\gamma_{int} d^4} \tag{2.13c}$$

$$\tilde{B}_S = \frac{\kappa_1 + \kappa_2 + \kappa_3}{\gamma_{int} d^4} \tag{2.13d}$$

The edge line tensions γ_L of membrane pores were also calculated. γ_L refers to the energy penalty for exposing a broken edge of the membrane to the solvent. To measure the edge line tension, a cylindrical coordinate system was used in the SCFT calculations. In this model, angular symmetry is assumed, while the spatial dependence in the radial (r) and axial (z) directions can vary. The condition of a closed surface was also relaxed. The edge line tensions were calculated by comparing the free energy of different pore radii produced with the SCFT with the theoretically expected results from the Helfrich description. Since the pore radius is related to the edge length as $l = 2\pi R$, where R is the radius of the pore, a calculation of the edge line tension is simply,

$$F^{Pore}A = 2\pi\gamma_L R \tag{2.14}$$

The slope of a linear fit will give the edge line tension γ_L. The edge line tension is rescaled as,

$$\tilde{\gamma}_L = \frac{\gamma_L}{\gamma_{int} d} \tag{2.15}$$

which can be used to understand the effect microscopic system parameters have on pore formation.

The methods described in this chapter were applied to a variety of system configurations to elucidate how the microscopic system properties effect the macroscopic properties. In the next chapter, the results for an AB diblock copolymer, C homopolymer system is presented and discussed. In later chapters, a more complicated system is employed using a blend of two chemically distinct diblock copolymers (AB/CD) mixed with an E homopolymer solvent. The last chapter is dedicated to calculating the edge line tension γ_L of two-component diblock bilayer systems.

Chapter 3

Single-Component Bilayers

This chapter is focused on the calculations of the bending moduli for a system of AB diblock copolymers and C homopolymers (AB/C). To begin, a description of how the moduli are attained is presented, then the results for the low-order moduli (κ_M, κ_G) are shown. After the second-order terms are determined for a variety of system parameters, the high-order moduli (B_c, B_s) are calculated. A condition is defined for the validity of the linear Helfrich model for systems exhibiting high curvatures and comparisons are made between the low-order and the high-order models. A critical curvature phase diagram is presented which gives a reference for what set of microscopic system parameters require a higher order model to describe the bending energetics.

To determine the bending moduli of the bilayer system, the first step is to stabilize a bilayer membrane in the computation cell. The computation cell is typically $12R_g$ in size for the one-dimensional case, with a discretization grid of 120 points. This gives a spatial resolution of $dx = 0.1R_g$ which is enough to capture all the details of the bilayer. By careful adjustment of the chemical potentials and initial fields, a

stable bilayer membrane is created, as depicted in Figure 3.1.

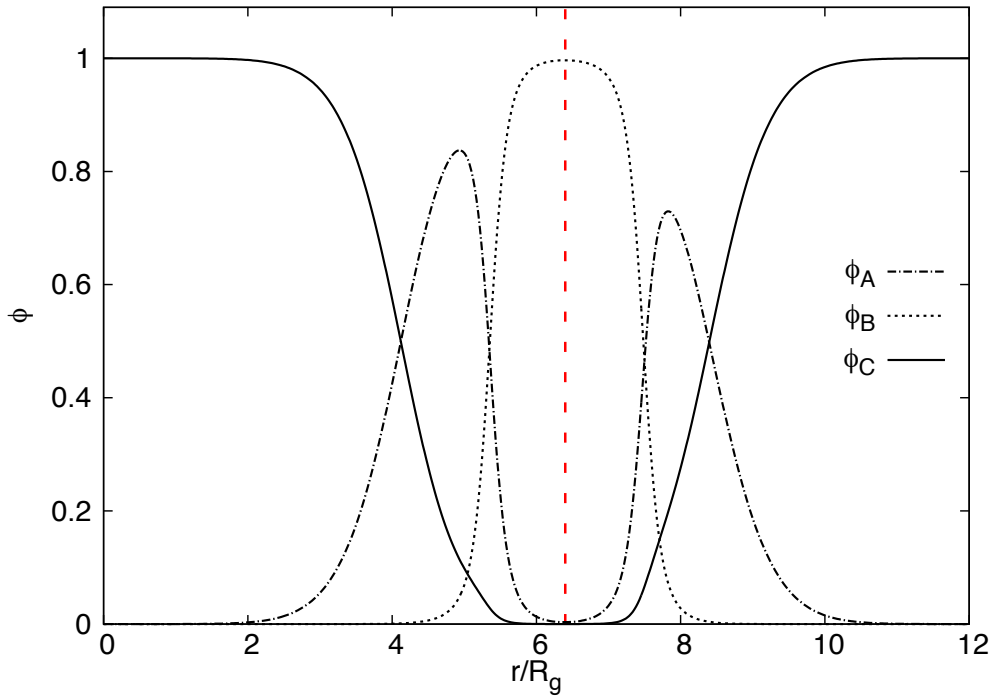

Figure 3.1: A typical concentration profile for a curved bilayer membrane. The hydrophobic tail regions (ϕ_B) are shielded from the solvent (ϕ_C) by the hydrophilic head groups (ϕ_A). The average thickness of the bilayer is typically $d = 4.3R_g$, which is used as the curvature length scale in the system. The vertical (red) line shows the maxima of the hydrophobic concentration, used to define the bilayer neutral plane.

To calculate the various bending moduli, the free energy as a function of the system curvature is calculated. This is done by maintaining the simulation cell size ($12R_g$) while adjusting the distance between the centre of the geometry and the calculation cell inner edge, denoted as r_0 (Fig. 3.2).

To study cases with high curvatures, a consistent measure of the bilayer radius must be used. In all cases, the maximal concentration of the hydrophobic groups (ϕ_B), which defines the centre of the hydrophobic core was used. In the case of an

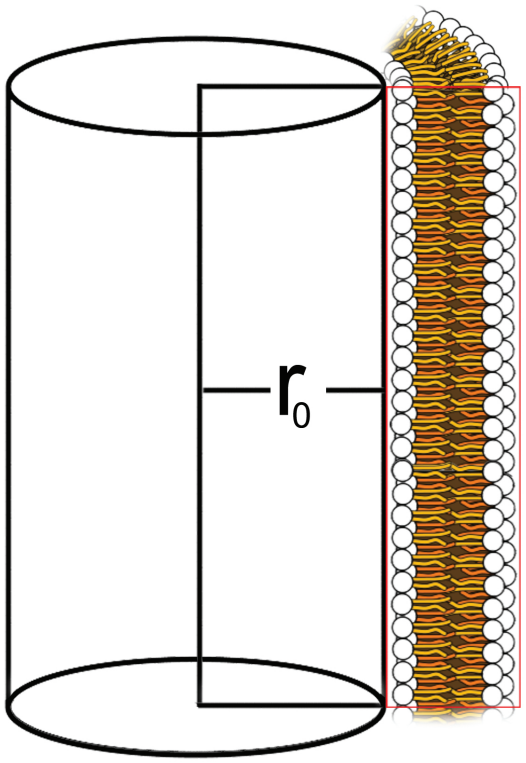

Figure 3.2: Diagram showing the radius of a cylindrical geometry to the inner edge of the computation cell (shown in red). This distance r_0 can be adjusted to allow for a wide variety of curvatures without the need to change the computation cell.

AB diblock system, the condition can be written as $\partial\phi_B(r)/\partial r = 0$, which is shown as the vertical (red) line in Figure 3.1. Using the results calculated with the SCFT, the free energy as a function of curvature is found. An example of such data is shown in Figure 3.3. The free energies found from the SCFT are then used to calculate the bending moduli of the system by fitting the data to the low and high-order bending models.

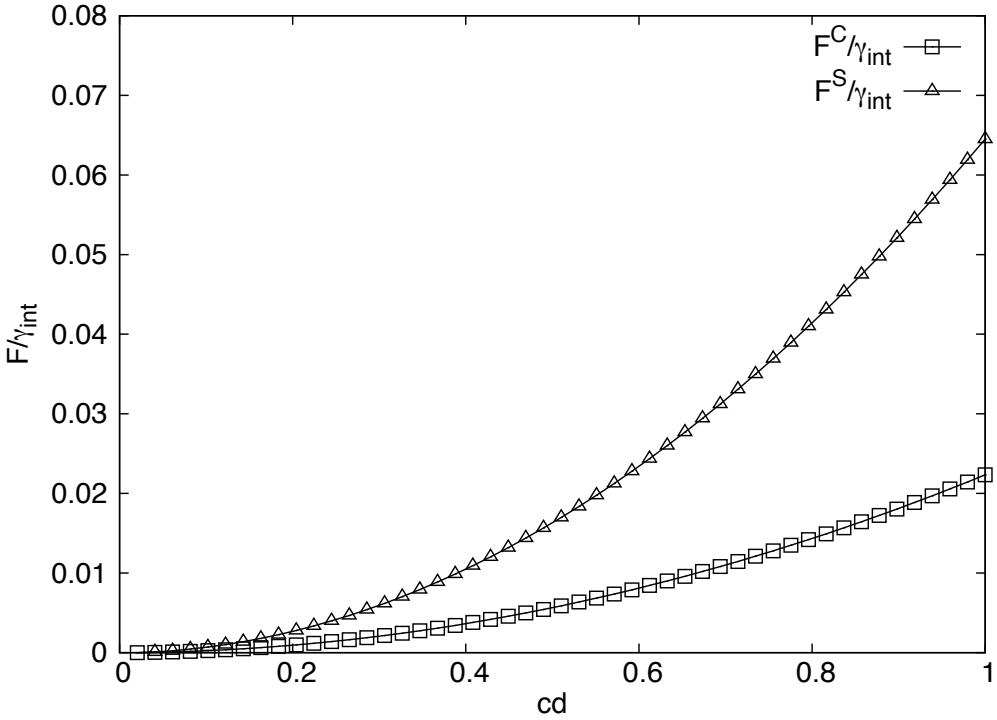

Figure 3.3: Free energy as a function of the scaled curvature for the cylindrical (F^C) and spherical (F^S) geometries. At $cd = 0$ the bilayer is essentially flat, regardless of the geometry, and attains the planar value of zero energy. For cases of low curvature $cd \approx 0.0 - 0.5$, there is a quadratic relationship between the curvature and free energy. In systems of high curvature $cd > 0.5$, fourth-order terms enter the free energy and deviations away from the linear Helfrich model occur.

3.1 Second-Order Moduli (κ_M, κ_G)

To determine the bending modulus κ_M and the Gaussian bending modulus κ_G, a quadratic function was fit to the free energy curves shown in Figure 3.3 in the low curvature regions ($Cd < 0.5$). It is assumed that at low curvatures, the high-order bending contributions have an insignificant contribution to the free energy, and that the lower order terms dominate. These fits were done over a large parameter space in order to understand the effects of hydrophilic length fraction f_A, interaction strengths

χN and solvent length κ, on the bending moduli of the system. The first results presented show the effect of chain fraction length of the hydrophilic group (f_A) and the interaction strength ($\chi_{AB}N = \chi_{BC}N = 25, 30, 35$). For these results, the homopolymer length was the same as the AB diblock ($\kappa = 1$), and the interactions between the hydrophilic groups and solvent are neutral ($\chi_{AC}N = 0$).

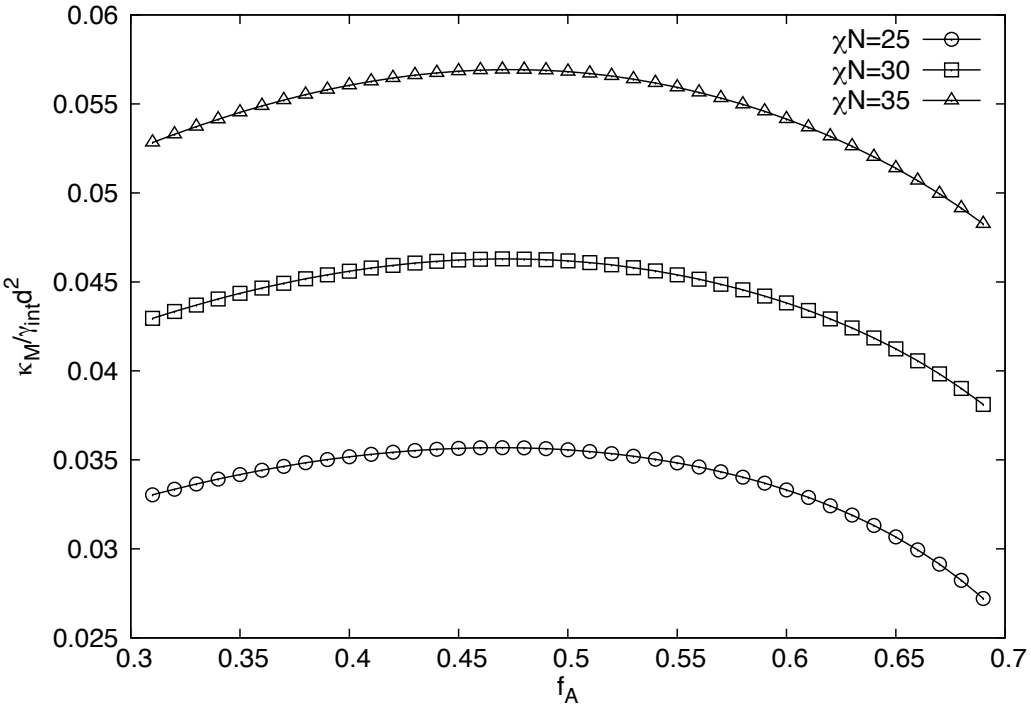

Figure 3.4: Bending modulus (κ_M) for chain fractions of $f_A = 0.3{-}0.7$, for interactions of $\chi_{AB}N = \chi_{BC}N = 25, 30, 35$. The results show that the chain fraction does not have a dramatic effect on κ_M, while an increase in interaction strength reinforces the mechanical strength of the bilayer.

The results in Figure 3.4 show that the bending modulus depends only slightly on

the chain fraction length f_A, but increases with the interaction parameter χN. The results also show that the modulus is maximized for symmetric or almost symmetric chains ($f_A \approx 0.5$). This slight asymmetry is due to the solvability of the various groups. It is much more difficult for the C homopolymers to hydrate the hydrophobic chains compared to the hydrophilic head groups. In the short head case ($f_A < 0.5$), a high degree of homopolymer overlap occurs between the hydrophobic core and the homopolymer solvent. When this occurs, the overall reduction in the packing density of the chains leads to a more flexible membrane, which lowers the rigidity. In the long head region ($f_A > 0.5$), a shorter hydrophobic chain length causes a reduction in the hydrophobic core thickness, which has been shown to reduce the rigidity [42]. By increasing the interaction parameter, the solvability of the hydrophobic core is reduced and allows for more densely packed chains which thickens the membrane and increases the bending modulus.

The Gaussian bending modulus κ_G was calculated for the same set of parameters shown in Figure 3.4. The results presented in Figure 3.5 shows interesting behaviour when the length fraction (f_A) changes.

The first feature is that κ_G is a monotonically decreasing function of the chain fraction f_A, and at $f_A \approx 0.4$ the modulus crosses zero. Another result is that an increase in χN increases the magnitude of the Gaussian modulus. The free energy contribution from the Gaussian curvature goes as,

$$F_G = \kappa_G \int dAG = 2\kappa_G \pi \chi(g) = 2\kappa_G \pi (2 - 2g) \tag{3.1}$$

where the Gauss-Bonnet theorem was used. This shows that for a fixed topology, the free energy contribution is invariant. The $\chi(g) = 2 - 2g$ is the Euler characteristic,

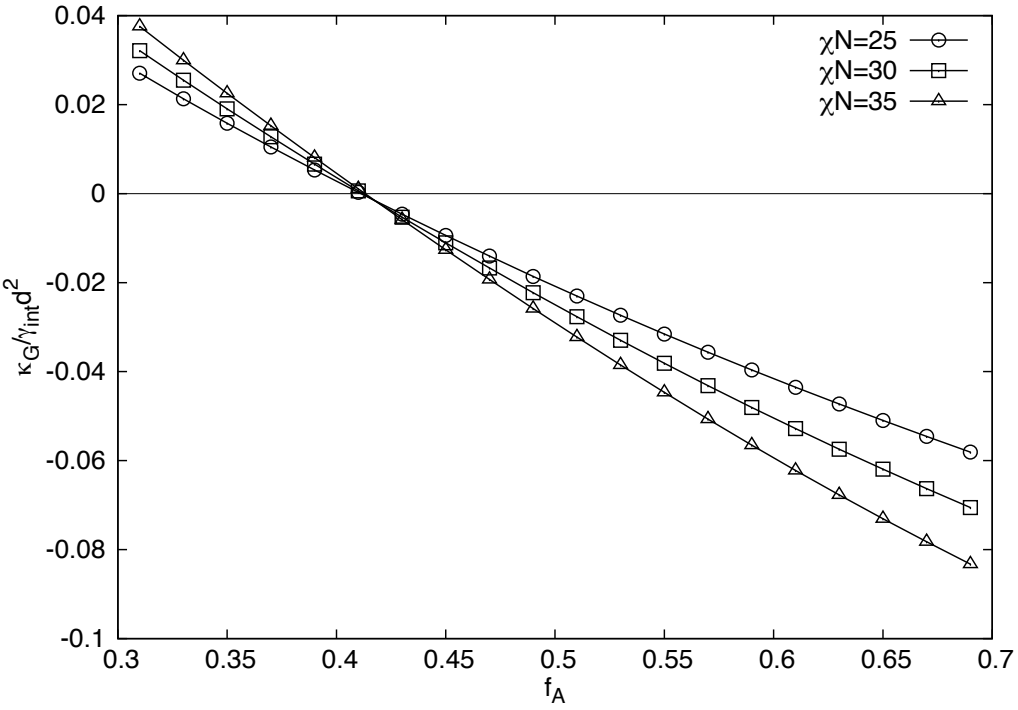

Figure 3.5: Gaussian modulus (κ_G) for chain fractions of $f_A = 0.3 - 0.7$, for interactions of $\chi_{AB}N = \chi_{BC}N = 25, 30, 35$. A transition from positive modulus values to negative occurs at $f_A \approx 0.4$, which signifies a change in the preferred topology.

where g is the genus (number of handles) of the surface. In the case of spheres, $g = 0$ and $F_G = 4\kappa_G\pi$ which is independent of the overall configuration of the surface. This is why in many studies, the Gaussian modulus is treated separately. Experimental and theoretical studies have been performed to calculate this value in the past, however due to the complex nature of the system, experimental work has been limited [10,12]. In the region where $\kappa_G < 0$, it is clear that the spherical geometry reduces the free energy of the system by making $F_G < 0$. After the transition from negative to positive, the Gaussian curvature term favours the formation of handles (perforations) in the surface, which can be related to pore formation, fission/fussion events and other biological processes.

A value commonly quoted in the literature is the ratio κ_G/κ_M. A plot of this ratio is shown in Figure 3.6. It has been shown that in biological systems, the ratio $\kappa_G/\kappa_M \approx -1$ [24]. Comparing to the calculations, this value is found at $f_A \approx 0.57$, which allows for a rough comparison of the simplified model to real biological systems. It may be useful to draw conclusions for system parameters that match this condition if comparisons to real membranes are to be made.

The homopolymer solvent has thus far been the same size of the AB diblock ($\kappa = 1$), and has the same chemistry as the hydrophilic portion of the diblock ($\chi_{AC}N = 0$). This means the above discussion was focused on an AB diblocks mixed with A homopolymers. The effect of the solvent is well known to have important implications on both the membrane and biology of living systems. For example, in biological systems a chemical potential gradient across the membrane drives many processes such as muscle contractions and neural signalling [8]. Therefore, understanding the effects that the solvent has on the membrane is important. The first step is to

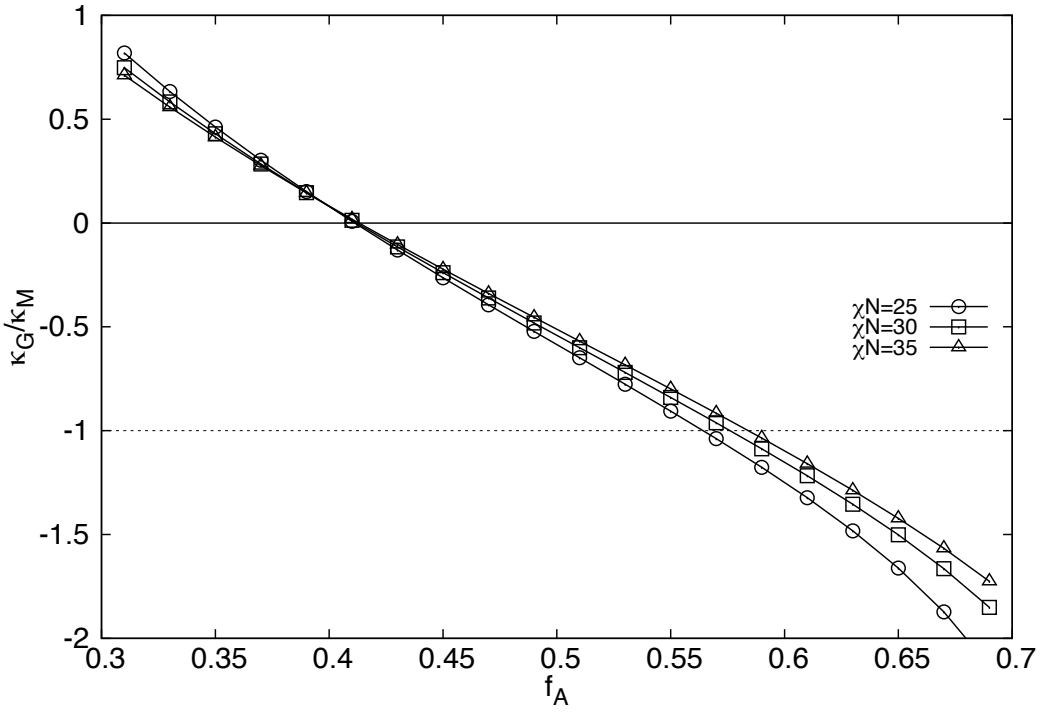

Figure 3.6: Ratio of the Gaussian modulus κ_G relative to the bending modulus κ_M. Biological membranes have been shown to take on a value close to $\kappa_G/\kappa_M = -1$. This result can be used to compare the simplified model presented with biological membrane systems.

understand the effect that immiscible solvents have on the bending modulus κ_M and the Gaussian modulus κ_G. This is performed by increasing the Flory-Huggins interaction parameter between the hydrophilic A block of the AB diblock and the C homopolymer ($\chi_{AC}N \neq 0$). In all cases, the interactions between the hydrophobic B chains are $\chi_{AB}N = \chi_{BC}N = 30$. The first result in Figure 3.7 shows the effect of solvent interactions on the bending modulus (κ_M).

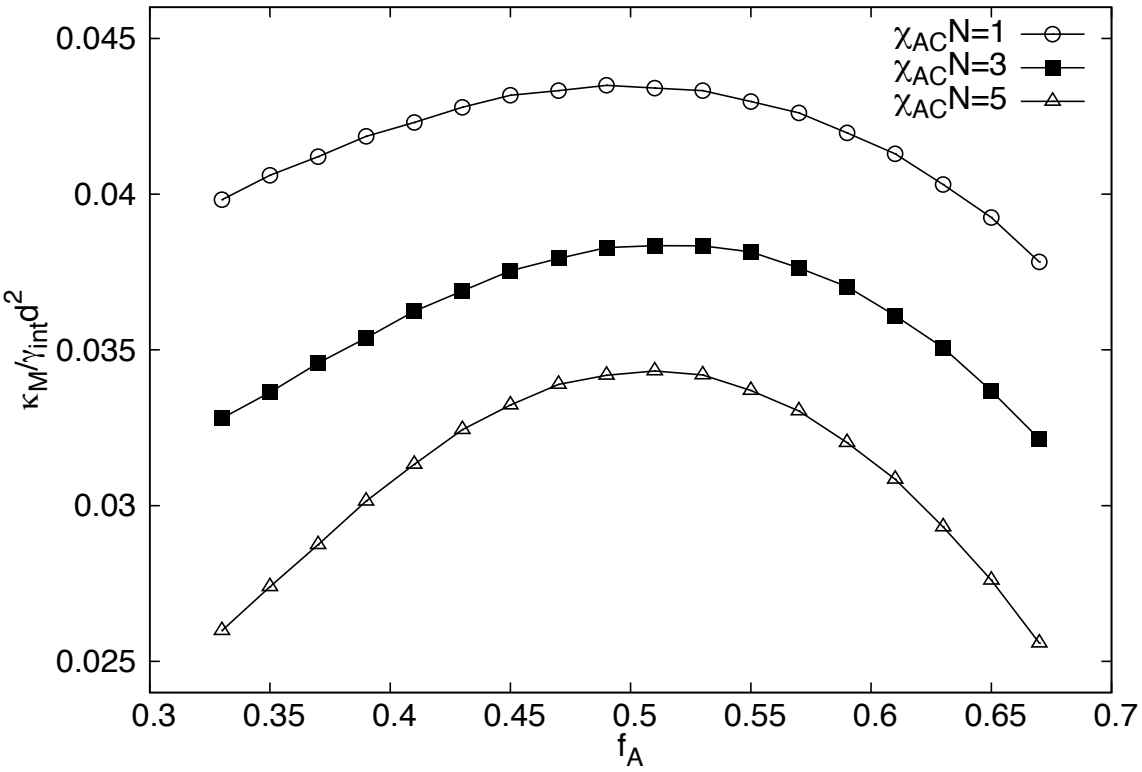

Figure 3.7: Bending modulus (κ_M) as a function of the hydrophilic chain fraction f_A for different solvent interaction values. Increasing $\chi_{AC}N$ causes a decrease in the rigidity of the chain.

As $\chi_{AC}N$ increases, the immiscibility between the solvent and head groups increases. Figure 3.7 shows that as $\chi_{AC}N$ increases, a significant decrease of the bending modulus occurs even for relatively small parameter values ($\chi_{AC}N$). This is due to new packing constraints on the A chains. Since the solvent is no longer able to hydrate the head groups as efficiently, this causes the head groups to pack more closely and increase the lateral area occupied by the chains. This causes an overall reduction in the rigidity. This phenomenon has also been seen by the Oversteegen group, where a similar effect due to the solvent interaction occurred. Oversteegen *et al.* [14] found that along with the reduction in the bending modulus for a given set of system parameters (f_A, $\chi N, \kappa$), an increase in the Gaussian modulus κ_G was also present. Comparing the results of Ref. [14] with those in this study, it is clear that a similar trend occurs. Figure 3.8 shows the results for the Gaussian bending modulus κ_G. Similar to the results of Overteegen *et al.*, an increase in the interaction $\chi_{AC}N$ leads to an increase in the Gaussian modulus. The results presented show that small changes in the solvent parameters can have a drastic effect on the stability of certain morphologies. For modest interaction strengths ($\chi_{AC}N \approx 3$), it is seen that at all values of f_A, the Gaussian modulus is positive. As discussed previously, $\kappa_G > 0$ means that it is energetically more favourable to form handles in the membrane rather than have a closed spherical bilayer. This can also make the formation of pores and necks more favourable, as these topological changes reduce the overall free energy.

Another solvent property studied is the homopolymer relative length fraction κ. The main effect the length of the solvent has on the membrane bending moduli is the ability for the solvent to penetrate the bilayer. When the solvent is smaller than the diblock length ($\kappa < 1$), the solvent can more easily penetrate the head groups of

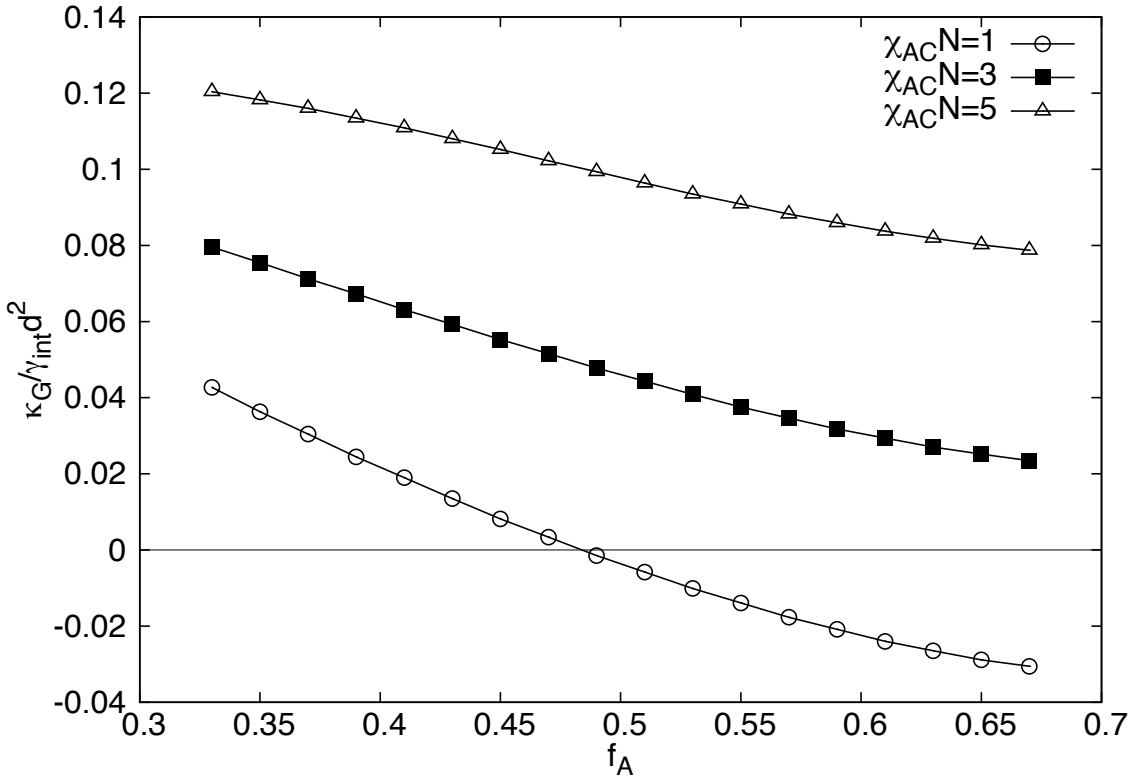

Figure 3.8: Gaussian bending modulus (κ_G) as a function of the hydrophilic chain fraction f_A for different solvent interaction values. Small changes in the solvent chemistry leads to an upwards shift in κ_G. For $\chi_{AC}N > 3$, the Gaussian modulus is strictly positive which may promote non-spherical topologies.

the bilayer, while the opposite effect occurs for $\kappa > 1$. The results for the bending modulus κ_M are shown in Figure 3.9. When the solvent can more readily hydrate the bilayer, an increase in the rigidity of the membrane occurs. The physical arguments are similar to those discussed above where a reduction in solvent penetration caused an overall reduction in the strength of the bilayer. Another interesting result is the increase in the asymmetry of the rigidity maximum across the range of f_A. As mentioned before, this was thought to be due to the solvability of the homopolymer with the head groups of the bilayer, and these results support that claim.

The results for the Gaussian bending modulus (κ_G) follow the same expected trend (Fig. 3.10). When the hydration of the head groups is greater, κ_G shifts to more negative values. The opposite effect is also seen when the solvent length is increased, leading to less stable bilayers.

The results show that solvent conditions play a very important role in the mechanical properties of the bilayer membrane, perhaps even comparable to the membrane structure itself. Solvent conditions in biological membranes are known to have important roles in various biological functions. Even with the simplified model used in this work, the solvent has been shown to have very important effects on the membrane strength and structure. Exploring the effect of solvent gradients, composition and concentrations using this model in the future could have novel applications, such as exploring the effect protein inclusions have on the bilayer.

3.2 Fourth-Order Moduli (B_C, B_S)

The bending modulus κ_M and the Gaussian modulus κ_G found in the previous section are used to describe the bending energetics of low curvature membranes. In many

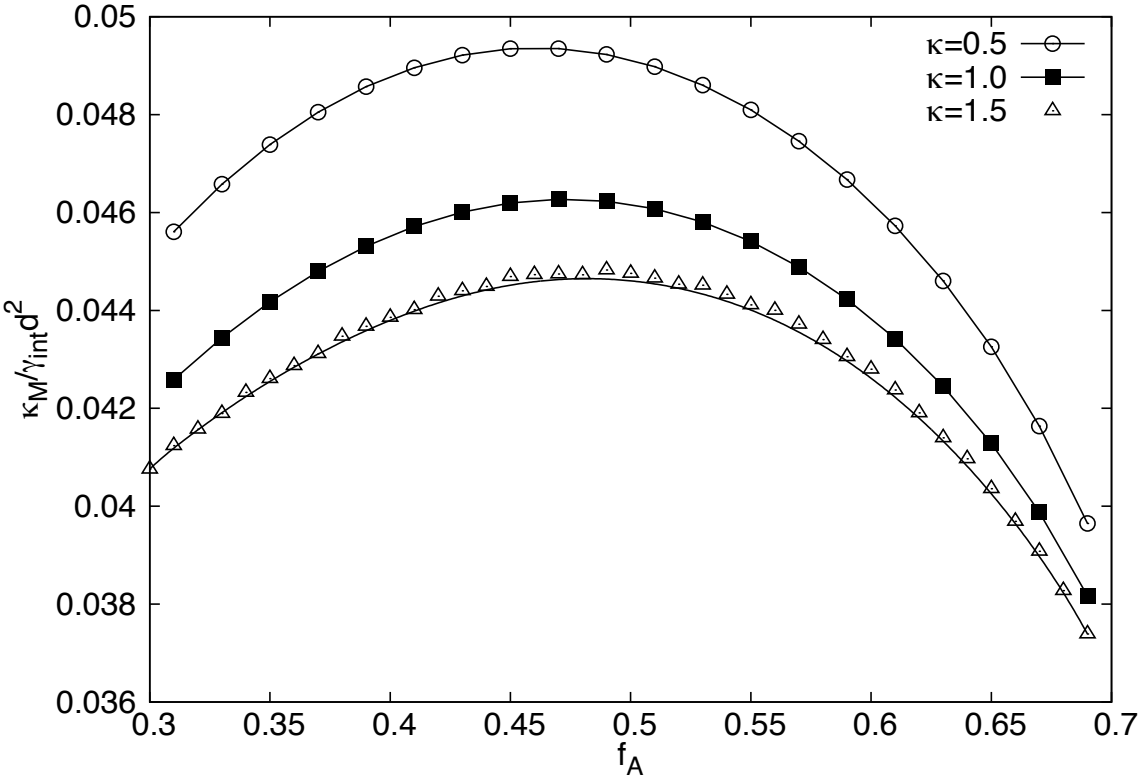

Figure 3.9: Bending modulus (κ_M) for a variety of homopolymer length fractions κ. When the homopolymer is longer than the AB diblock it is unable to hydrate the hydrophilic head groups leading to a decrease in the bending rigidity. The solvent also has an effect on the position of the maximal bending rigidity, leading to a more pronounced asymmetry.

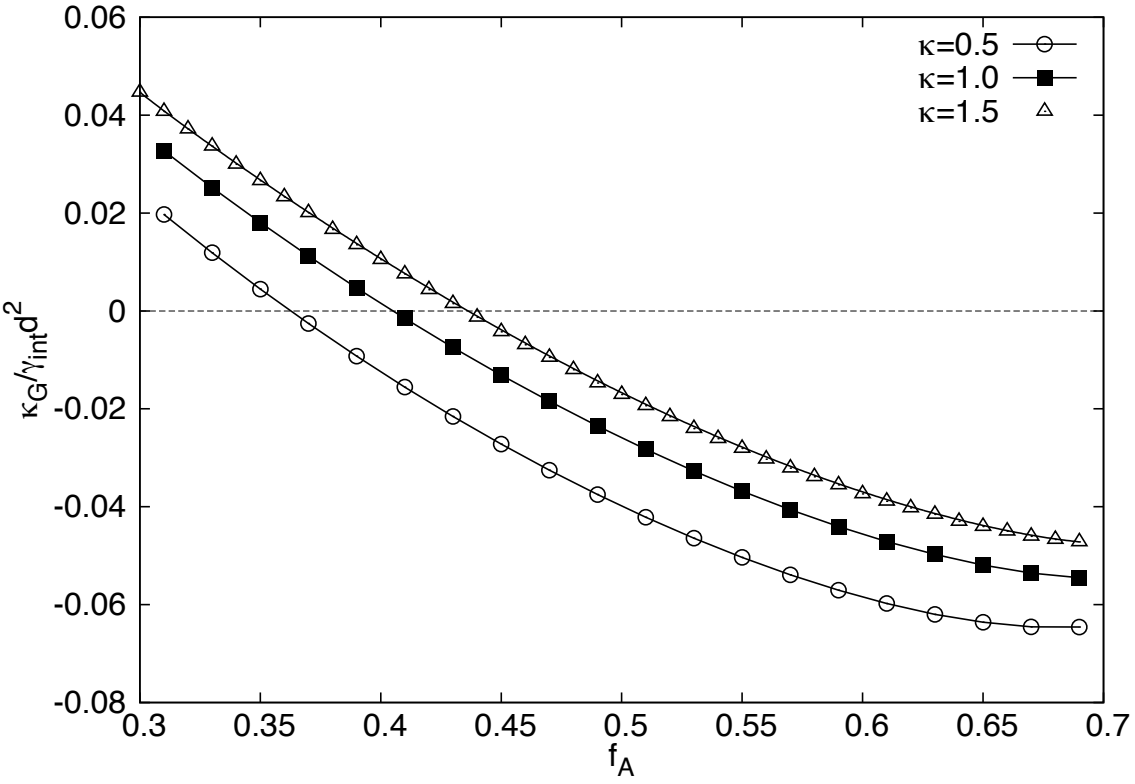

Figure 3.10: Gaussian bending modulus (κ_G) for different homopolymer length fractions κ. An increase in the homopolymer length shifts κ_G to more positive values and shifts the zero crossing transition.

biological systems and processes, regions of high membrane curvature are present. In highly curved membranes it is not known whether the Helfrich model can be used to accurately predict the bending energetics. In order to address this question, higher order moduli shown in Eq. (1.2) have been added to the bending free energy. Performing the SCFT calculations in high curvature systems allows for an understanding of the effect high-order terms have on the membrane energetics. As discussed earlier, there are not enough easily accessible geometries to determine the high-order moduli independently. Instead, linear combinations of the moduli are presented as $B_C = \kappa_1/16$ for the cylindrical fourth-order modulus and $B_S = \kappa_1 + \kappa_2 + \kappa_3$ for the spherical fourth-order modulus. The goal is to be able to understand the limitations of the standard Helfrich model. A systematic study of the bilayer membrane is done to outline where the linear elastic theory is able to accurately describe the energetics of the system. Calculations for an AB diblock, A homopolymer blend with solvent length $\kappa = 1$ and interaction parameters of $\chi_{AB}N = \chi_{BC}N$, and $\chi_{AC}N = 0$ for a variety of chain fraction lengths f_A is shown in Figures 3.11 and 3.12.

The results clearly shown that for highly curved membranes, the fourth-order moduli take on non-zero values. This means that higher order contributions to the free energy have a non-negligable effect on the system. The positive contribution is expected from B_C since it is just a scaled version of the fourth-order mean curvature contribution. The negative values found for B_S are interesting since they lead to a reduction in the free energy of the system at high curvatures. B_S contains both the fourth-order contributions of the mean curvature and the Gaussian curvature, and also the coupling between them. Understanding the importance of these contributions on the bending energy must also be addressed. Section 3.3 defines a condition to compare

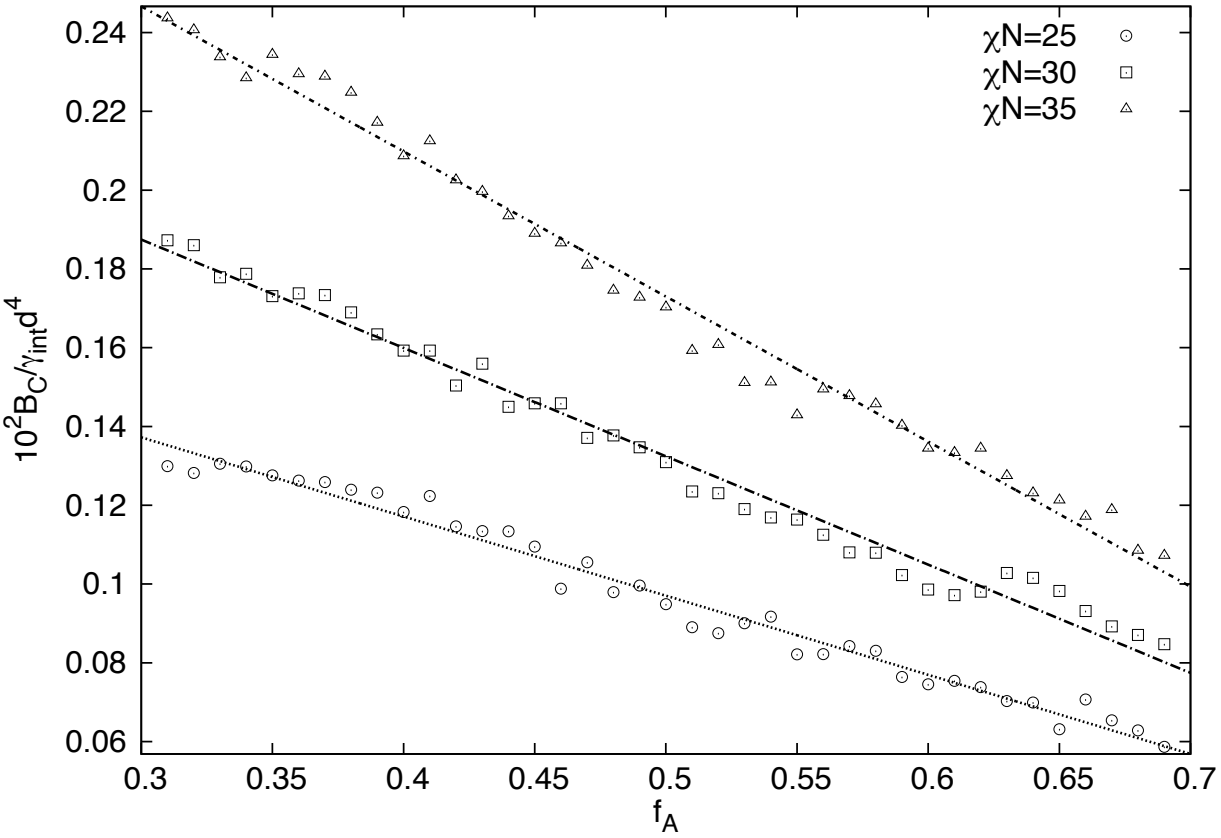

Figure 3.11: Fourth-order cylindrical bending modulus (B_C) for the AB/A system. Positive values are found for B_C which are expected since B_C is simply a high-order mean curvature scaling factor. A negative linear trend with f_A is also observed.

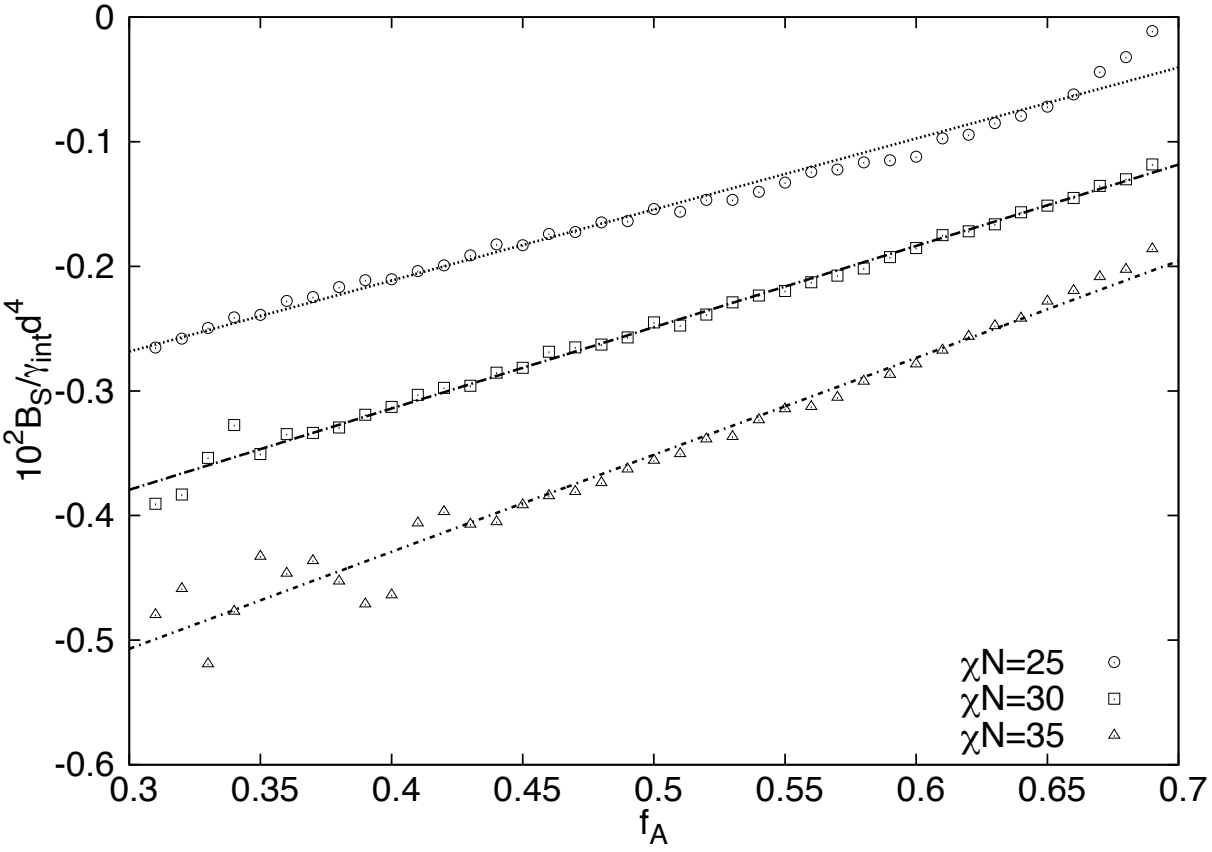

Figure 3.12: Fourth-order spherical bending modulus (B_S) for the AB/A system. The negative values show that the combination of the bending moduli cause a lowering of the free energy at high curvatures. It should be noted that B_S contains the coupling term κ_2 between the mean curvature M and the Gaussian curvature G.

the low and high-order models, and a critical curvature phase diagram is presented.

3.3 Limitation of the Helfrich Free Energy

Using the results for the bending modulus κ_M, Gaussian bending modulus κ_G, and the two fourth-order moduli B_C and B_S, the boundary separating the region where the fourth-order corrections are negligible can be determined. To determine this boundary, a physically relevant condition must be satisfied. In the current case, it is required that the absolute relative difference between the fourth-order free energy F_4 and the second order (Helfrich) free energy F_2 must be less than some critical energy. The relative free energy difference is written as,

$$\Delta E = \frac{|F_4 - F_2|}{F_2} \tag{3.2}$$

and must not exceed a critical value ΔE^*. Using the free energy expressions for the two models Eqs. (1.1,1.2), critical curvature values can be determined in both the cylindrical and spherical geometries. These critical curvatures are,

$$c_C^* = \sqrt{\frac{\kappa_M \Delta E^*}{2B_C}} \tag{3.3}$$

$$c_S^* = \sqrt{\frac{(2\kappa_M + \kappa_G)\Delta E^*}{B_S}} \tag{3.4}$$

which can be solved using the moduli found in the previous sections. As an example, it is assumed that the critical energy must not exceed $\Delta E^* = 2\%$. In Figure 3.13, a critical curvature phase diagram is shown for the f_A-cd plane.

In the filled regions, the system is accurately modelled using the linear elasticity theory (Helfrich model), while in unfilled regions one must apply the higher order correction terms to accurately calculate the system energetics. The results shown are meant to act as a guide for those studying relevant membrane systems of specific geometry and parameters. For example, if a calculation of the bending energy of a cylindrical tether is to be theoretically determined, it is likely that since this system exhibits high curvature, fourth-order moduli will contribute non-negligible energy to the system. The scale of the corrections depend on the accuracy needed, however the results show that consideration must be taken when applying these models to biological systems.

The results developed a systematic method for determining the bending moduli of diblock bilayer membranes in the framework of SCFT. This has been used to understand how the microscopic properties of the membrane effect the mechanical (macroscopic) properties. By utilizing this method, high curvature systems have been shown to be more accurately described using a higher order elastic model. Using these results, a validity region of the linear elasticity model has been determined. While this simple system has given many useful results, more complex systems can be easily evaluated using the SCFT framework. There is also interest in understanding the effect of mixtures of lipids within the membrane. The majority of biological membranes contain more than one type of lipid [43], and the role of these mixtures can give rise to interesting physics and mechanisms such as raft formation, curvature induced spontaneous curvatures, and edge stabilization of pores. The next chapter studies the effect of mixing two diblock species within the membrane.

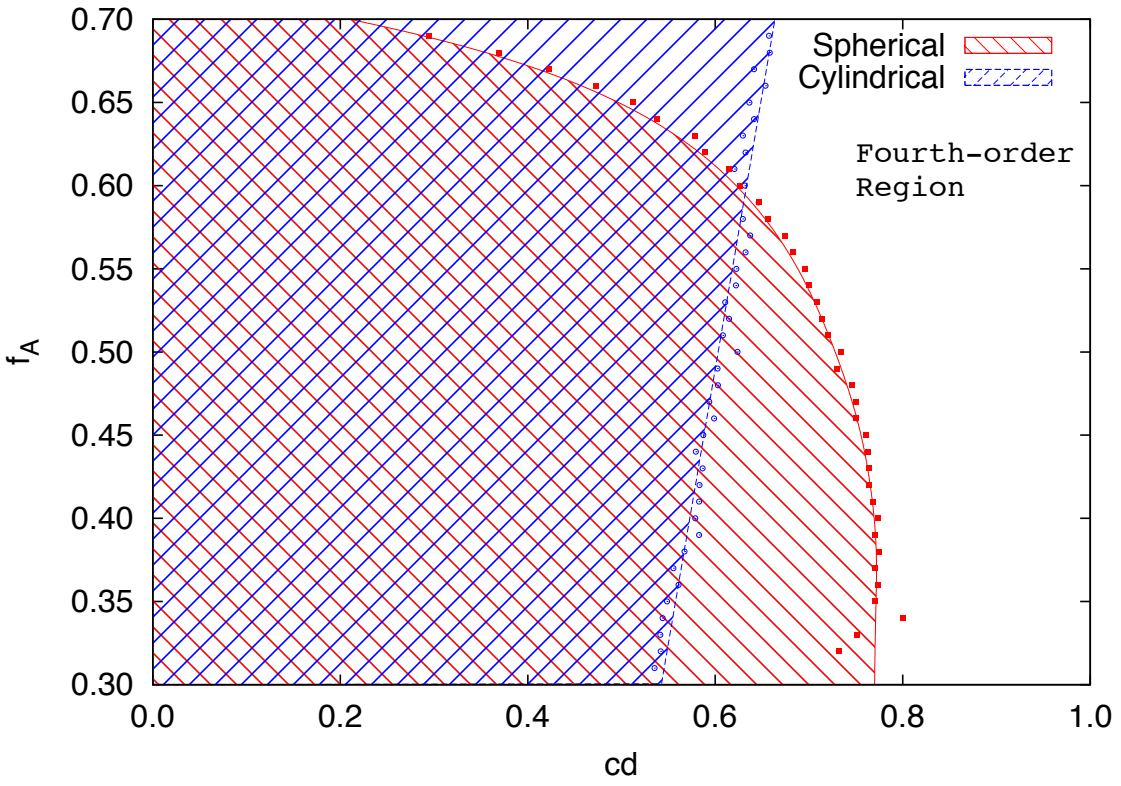

Figure 3.13: Critical curvature phase diagram for the hydrophilic chain fractions (f_A) and scaled curvature (cd). The filled regions show the parameter space where the bending energy is accurately described by the standard Helfrich description. In the unfilled fourth-order region, the high-order moduli must be added to describe the energetics of bending the bilayer membrane.

Chapter 4

Two-Component Bilayers

A system that has received some attention in the literature is the two-component lipid bilayer [11, 15, 16, 32, 44]. In Section 3.3, a simple description using a single diblock copolymer was used to model the lipid membrane, however in nature, lipid bilayers are composed of a large variety of different types of lipid molecules [43]. The system explored in this section is that of a mixture of AB and CD diblock copolymers blended with E homopolymers. Two-component membrane systems have a variety of interesting properties. Studies have shown that mixed bilayers can give rise to new stable morphologies in two-component giant unilamellar vesicles (GUVs) [32]. Lipid mixtures also allow for the possible formation of lipid rafts, as well as pore stabilization of highly curved membranes [8, 32, 33].

The goal is to understand how the bending moduli respond to mixing of two different types of diblocks within the membrane. This is done in the grand canonical ensemble by adjustment of the chemical potentials between the two diblock species.

To characterize the amount of each type of diblock in the membrane, an order parameter Ψ is defined as,

$$\Psi = \frac{\phi_1 - \phi_2}{\phi_1 + \phi_2} \tag{4.1}$$

where ϕ_p are the concentrations of the AB diblock ($p = 1$), and CD diblock ($p = 2$). A study on the effect of mixing two diblock with the same hydrophilic head length, but different hydrophobic tail lengths is performed. This system is similar to the one studied in Ref. [32], where the diblocks take on a cylinder (AB), and cone (CD) geometry. It is also argued that mixtures of different diblock geometries can lead to edge stabilization of membrane pores, which will be discussed later in this thesis. These types of systems may lead to phenomenon such as phase separation and raft formation, however in the current one-dimensional model, these details are not attainable. Using the same methods outlined in Chapter 2, the bending modulus κ_M is determined for the system.

4.1 Hydrophobic Mismatched Lipids

The system studied is a mixture of n_1 AB diblock copolymers of length fractions $f_A = f_B = 0.5$, and n_2 CD diblock copolymers with a hydrophilic length of $f_C\kappa_1 = 0.5$ and variable hydrophobic tail length f_D, where $f_C + f_D = 1$. In this definition, the relative length of the diblock is $\kappa_1 = (N_C+N_D)/(N_A+N_B)$. This states that the length of the head groups of both blocks are the same, however the D tail of the CD diblock reduces its overall length. In all cases studied, the length of the homopolymer solvent is the same as the AB diblock. The interaction parameters of the system are kept as $\chi N = 30$ between all hydrophobic and hydrophilic blocks and neutral otherwise.

This study is focused on short tail secondary polymers ($f_D < 0.5$), meaning that the CD diblock takes on a conical shape of various sharpness (Fig. 4.1). By careful adjustment of the chemical potentials between the diblocks, the relative concentration Ψ can be changed from $\Psi = 1$ for pure AB diblock bilayers, and $\Psi = -1$ for pure CD diblock bilayers. Any intermediate value of Ψ is a mixed system.

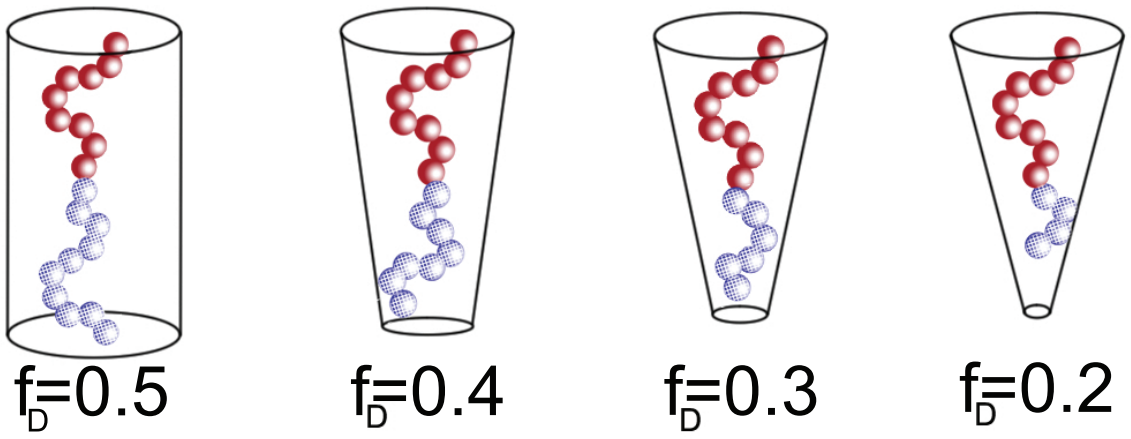

Figure 4.1: Diagram depicting the various conical shapes taken by the CD diblock copolymer. Smaller tail fractions (f_D), shown as hashed (blue) segments, give the diblock a more conical geometry.

The results for the bending modulus κ_M are presented in Figure 4.2 for a variety of length fractions (f_D). For pure AB diblock systems ($\Psi = 1$), all bending moduli have the same value, which are identical to those found for the symmetric ($f_A = 0.5$) system in Chapter 3. As the conical CD diblocks are added to the system, the bending modulus decreases monotonically until κ_M reaches the pure values for the CD system. For calculations with smaller f_D, the reduction is more pronounced. This is due to a reduction in the overall hydrophobic core, which is known to reduce the

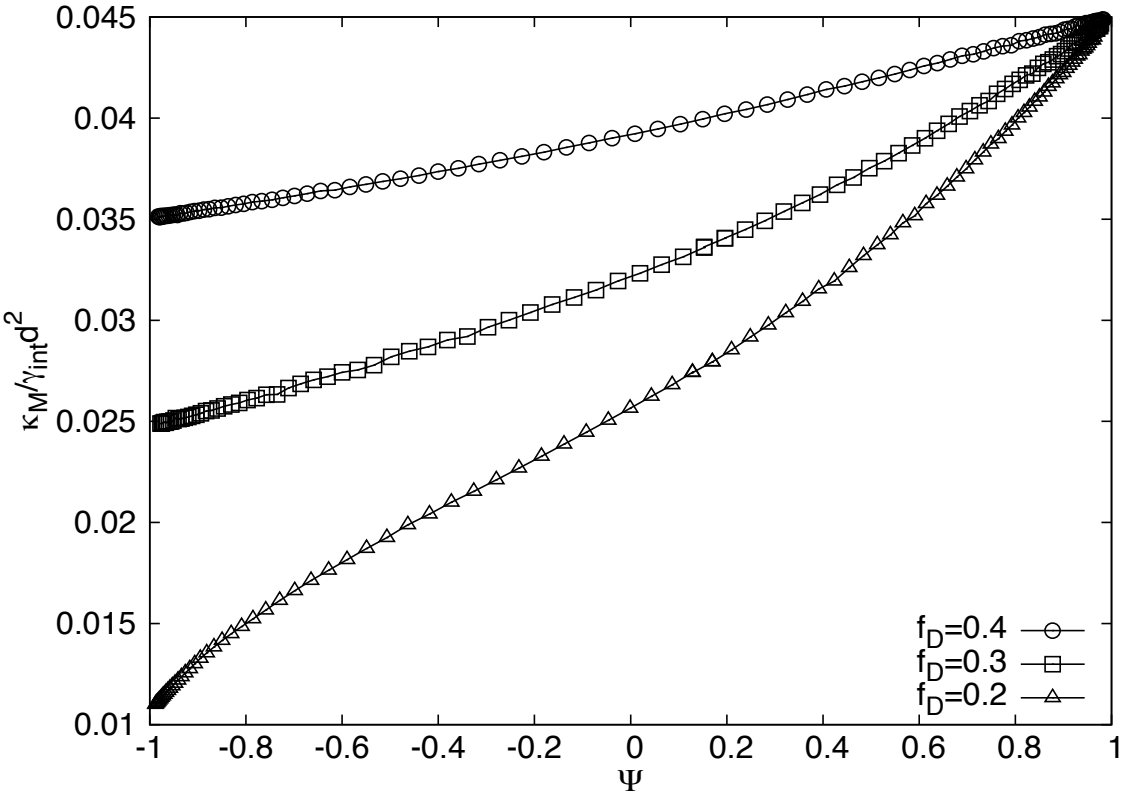

Figure 4.2: The effect of the mixing of short tail (CD) diblocks into a symmetric diblock (AB) bilayer, on the bending rigidity (κ_M) of the membrane. The result is shown for a variety of chain lengths (f_D). The values of $\Psi = 1$ correspond to pure symmetric diblock (AB), and $\Psi = -1$ are pure short tail (CD) dibocks.

bilayer stiffness. Similar results have been found in Szleifer *et al.* [15]. It should be noted that work by both Imparato (Ref. [11]) and Szleifer (Ref. [15]) have shown non-monotonic behaviour for mixtures membranes. In both cases, a minimum of κ_M was found for intermediate mixing ($-1 < \Psi < 1$) in systems where the chain density on each side of the bilayer was kept constant. This is known as the constant area model. Szleifer also looked at the effect of different monolayer interactions. It was shown that blocked exchange of lipids between the inside and outside monolayer, as well as free exchange (as done in this thesis) have the same qualitative behaviour, however the rigidity (κ_M) for blocked exchange was much larger. Therefore it is expected that the rigidity calculations in this thesis may be underestimated when compare to real systems. The results show that the bending modulus of the bilayer membrane can be continuously tuned by addition of diblocks of different bending moduli.

One interesting problem is the effect that mixed membranes have on the stability of pore formation. Chapter 4 is motivated by the work of Sakuma *et al.* [32], where they find interesting morphologies in two-component GUV mixtures of conical and cylindrical polymers.

Chapter 5

Line Tension of Bilayer Membrane Pores

In this chapter, the role of the microscopic structure of the diblocks on the edge line tension (γ_L) of bilayer pores is determined. In the past, experimental work on transient pore formation has been used to determine the line tension of pore formation in GUVs [45]. Calculations of the pore edge tensions have also been performed using molecular dynamics simulations [46], however direct calculation of the free energy is not available in these methods. From an industrial and biological stand point, it is important to have good understanding and control of pore formation in membranes. For example, polymeric nano reactors and artificial organelles depend on proper segregation between the interior and exterior environments [36]. In this section, a calculation of the edge line tension (γ_L) of the bilayer pore is done using the SCFT in a two-dimensional cylindrical coordinate system. The calculation uses the same methods as the previously presented results, however an increase in the geometric radius (r_0) is associated with the pore perimeter, as is depicted in Figure 5.1. Calculating the free

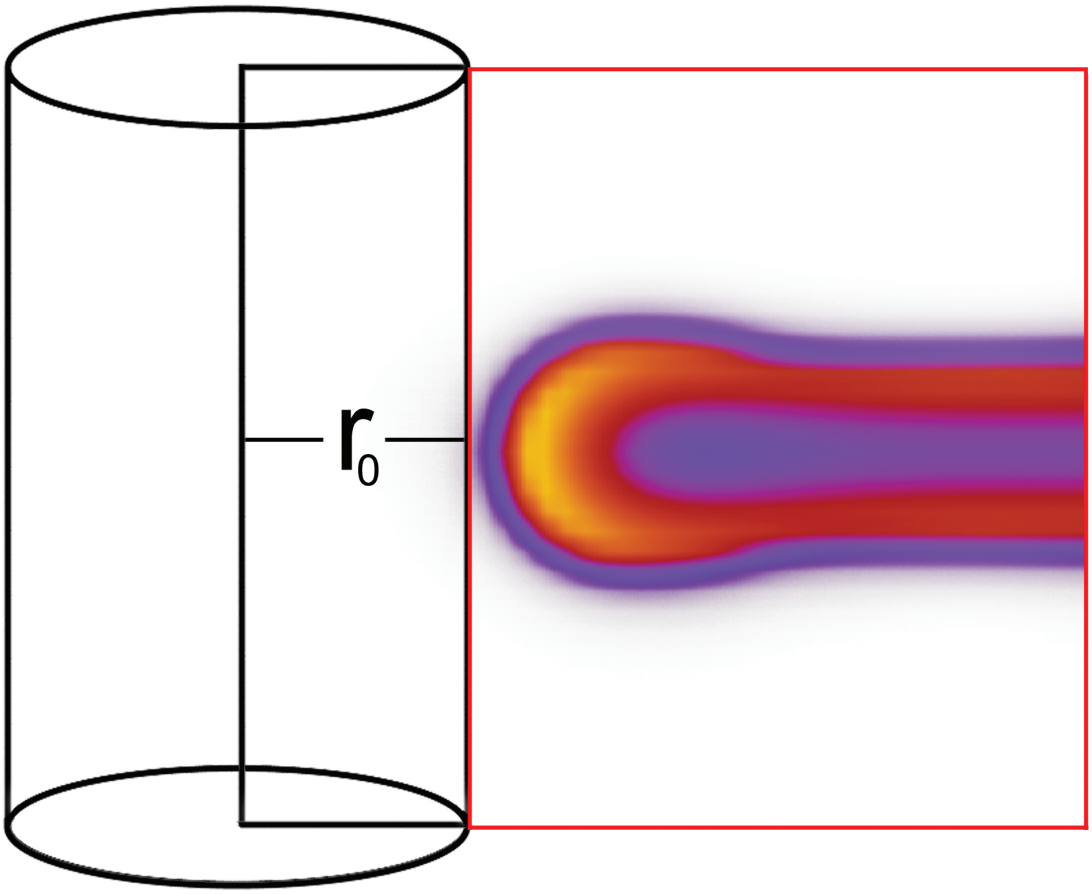

Figure 5.1: Schematic of pore formation in the cylindrical geometry. The radius from the centre of the geometry to the innermost edge of the computation cell is shown. Varying r_0 allows for pores of different sizes to be created, and their free energy calculated. Also shown is the typical concentration profile of the membrane pore, where the computation cell is the (red) box surrounding the profile.

energy of a pore system for a variety of geometries, gives a linear relation with the line tensions (Eq. 2.14). A representative free energy profile is shown in Figure 5.2. The line tension for a mixture of AB diblocks and C homopolymers as a function

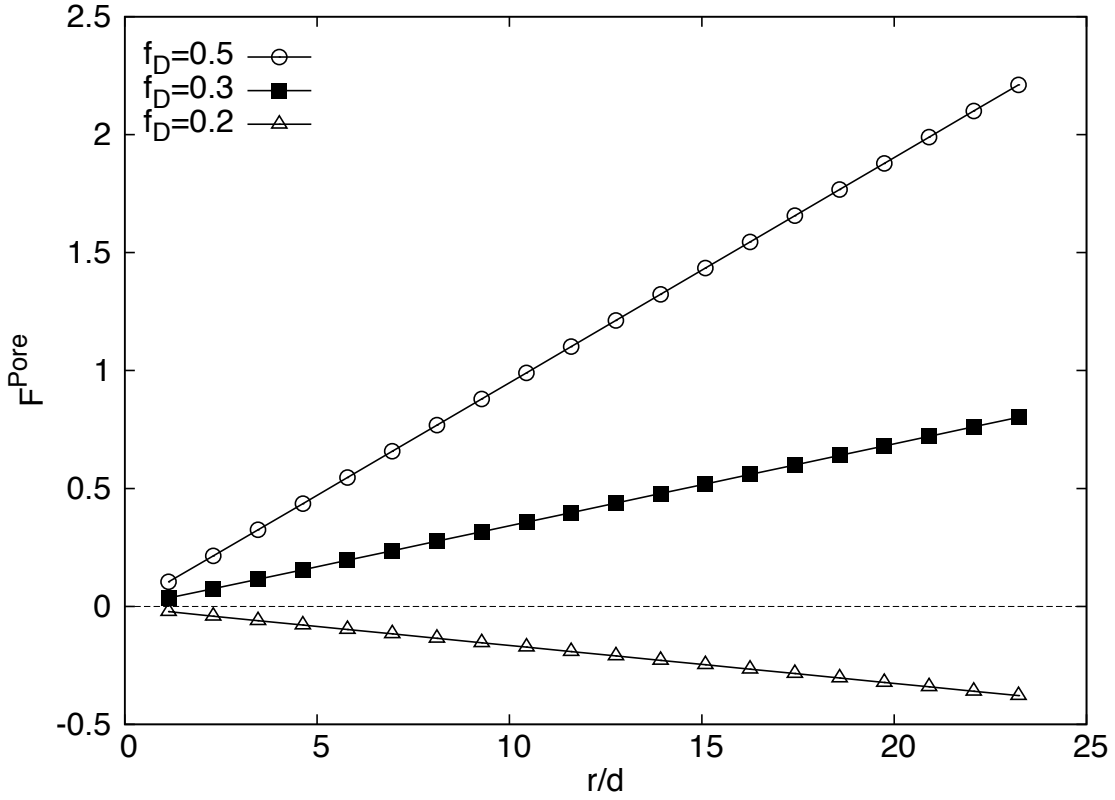

Figure 5.2: Free energy of the membrane pore as a function of pore radius (r/d). Depending on the length of the secondary diblock in the bilayer, the free energy can take shallower slopes. The linear relationship is used to extract the edge line tensions γ_L.

of the hydrophilic chain length f_A is first presented. This system is the same as in Chapter 3. The scaled line tension ($\tilde{\gamma}_L$) as a function of the hydrophilic chain fraction f_A is shown in Figure 5.3. A clear monotonically decreasing trend of $\tilde{\gamma}_L$ with chain fraction f_A is shown. The most striking result is that at $f_A \approx 0.6$, a crossover from positive to negative line tension occurs. This suggests that large head lipids lead to

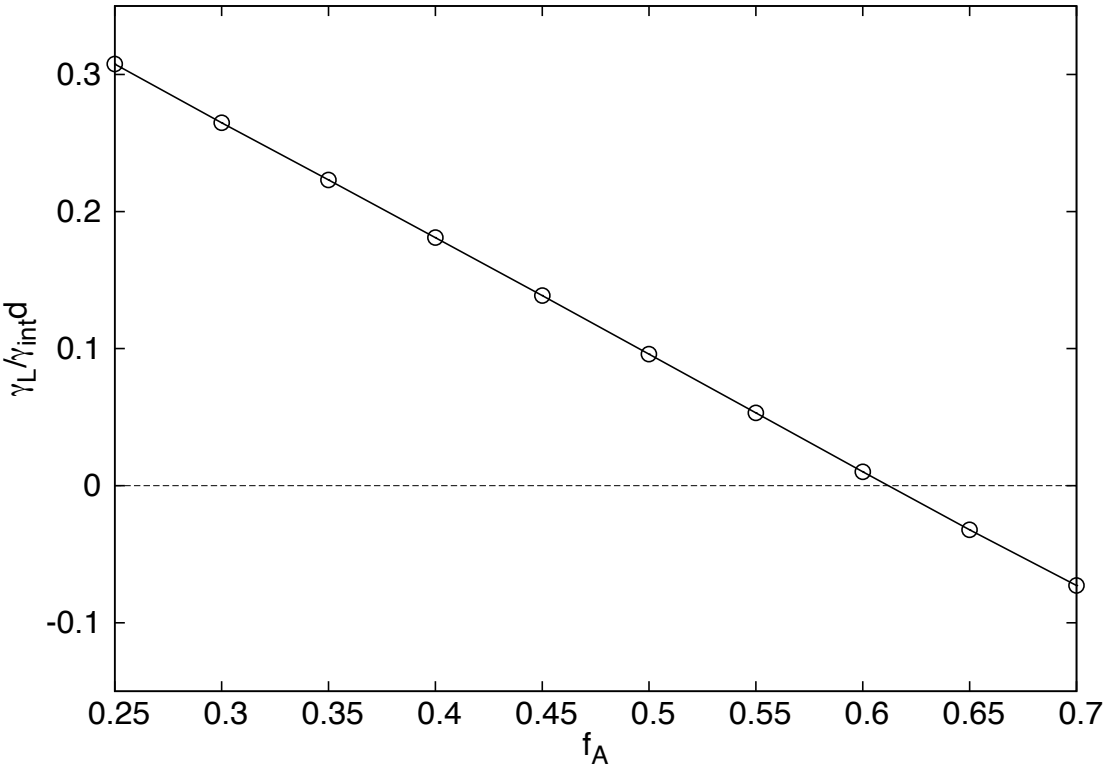

Figure 5.3: Scaled line tension ($\tilde{\gamma}_L$) as a function of the hydrophilic chain fraction (f_A). The line tension is a monotonically decreasing function with chain fraction and has a zero transition at $f_A \approx 0.6$. Negative line tensions can lead to stable pore formation in the bilayer membrane.

stable pore formation and can be used as edge stabilizing agents. By extending the system to include a second diblock into the bilayer (AB/CD diblock system), the effect of mixing the large head diblocks can be studied.

This final section studies the effect of mixing geometrically different diblocks (conical vs. cylindrical), and how they effect the edge line tension of membrane pores. It is expected that the addition of large headed (conical) diblocks into the membrane should reduce the edge line tension leading to a more stable pore. The results for this are shown in Figure 5.4.

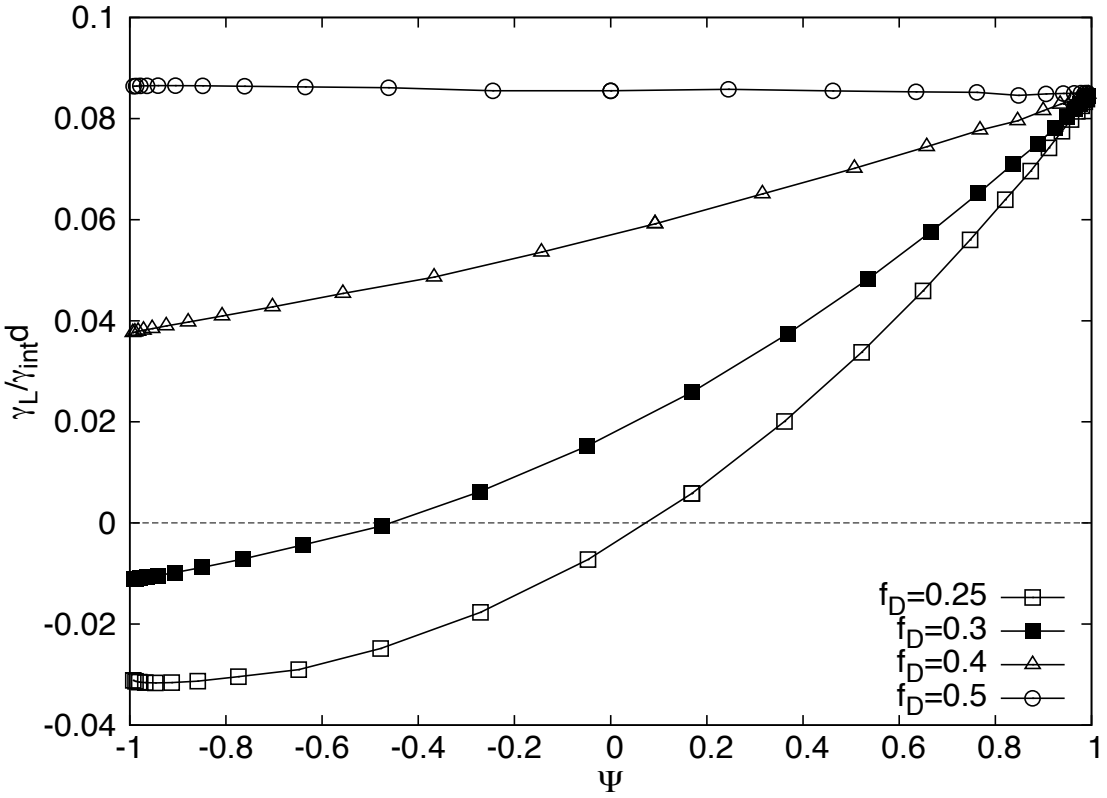

Figure 5.4: Edge line tension ($\tilde{\gamma}_L$) as a function of relative diblock concentration (Ψ) for a variety of secondary diblock geometries. More conical shaped diblock correspond to smaller hydrophobic tail segments (f_D). The addition of conical diblocks reduces the line tension of the pore. For very short tailed diblocks ($f_D < 0.3$), mixtures can lead to negative line tensions, making pore formation favourable.

The results show that as f_D is reduced, the line tension of the system is also lowered. For the CD diblocks of $f_D < 0.3$, negative line tensions are found. In general, the smaller the f_D, to achieve the same reduction in line tension, less concentrated mixtures are needed for more conical secondary diblocks. The mechanism behind this is rationalized by looking at the concentration profiles of the membrane pore. A density profile from the SCFT solutions is shown in Figure 5.5. The image shows the concentration of the conical diblock (CD) as if forms a membrane pore. The density profile shows that there is a large concentration of these diblocks near the pore edge, which shows that pore edge phase separation is occurring in the system. A clear view of this is shown in the $3D$ image representation where the dark (blue) region show an increase in the CD diblock (cone) concentration.

The ability for the pore to phase separate is driven by the complimentary geometry taken by the CD diblock. Naturally, such conical diblocks would try to from a micellar morphology, however since they are mixed in the bilayer, this cannot be achieved. To minimize the free energy, they aggregate to the regions of complementary curvature, in this case the pore edge, which results in a reduction of the system free energy as well as the line tension of the pore. This also has a relieving effect on the cylindrical blocks, as they no longer are penalized by high curvature at the membrane edge. To quantify the amount of edge separations, Figure 5.6 shows the concentration of each diblock type as a function of the radial coordinate. It is clear from the plot that edge separation is occurring. These results show that simply by mixing different polymer lengths, a drastic reduction in the edge line tension can be observed. From a biological stand point, this is perhaps a reason that cell membranes contain many different lipid components. Reordering of the lipid bilayer in certain situations to

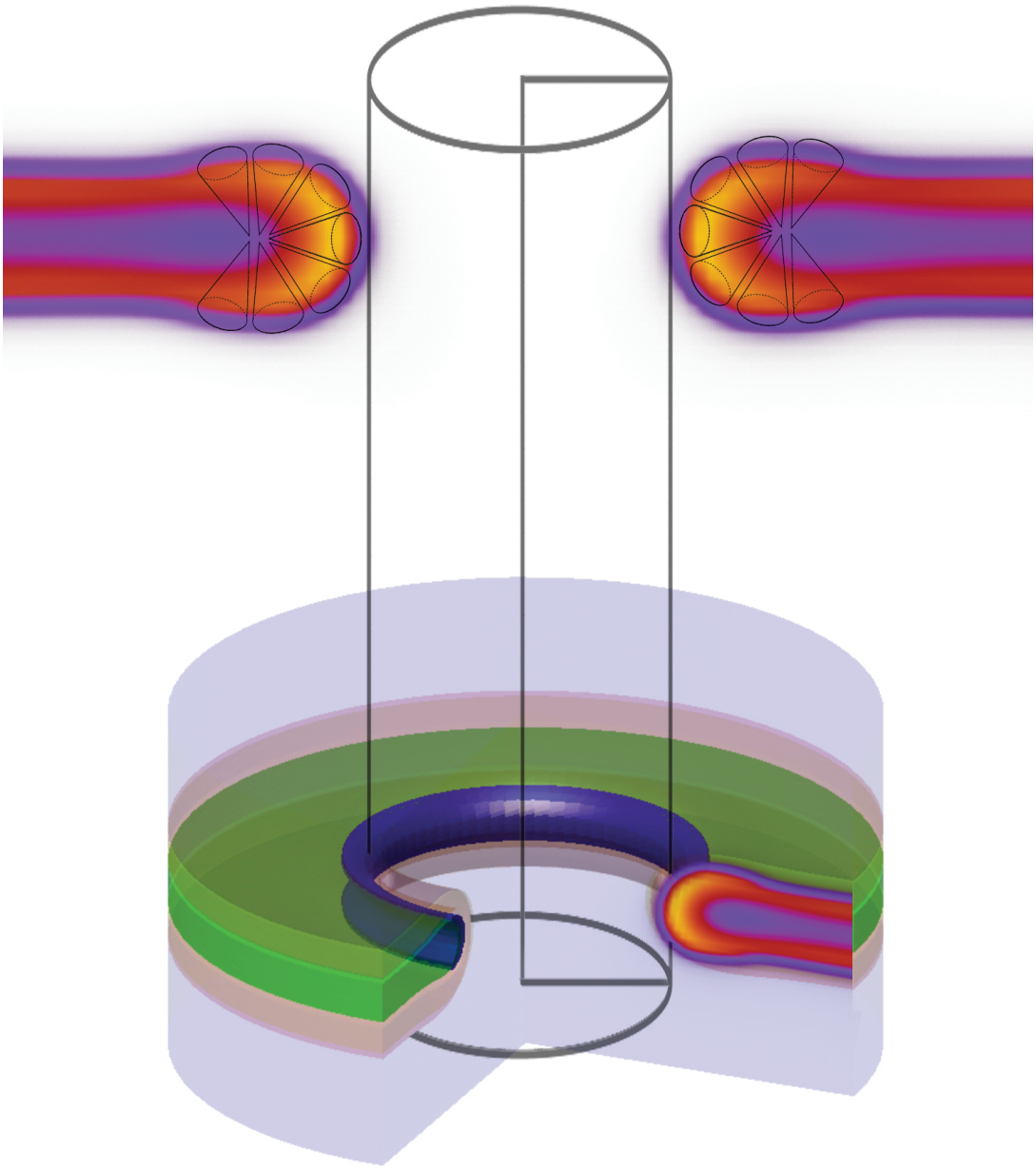

Figure 5.5: Concentration profile of the secondary conical CD diblock forming a membrane pore. The diblocks at the edge are represented as cones. The $3D$ representation shows edge phase separation of the conical diblock (dark/blue).

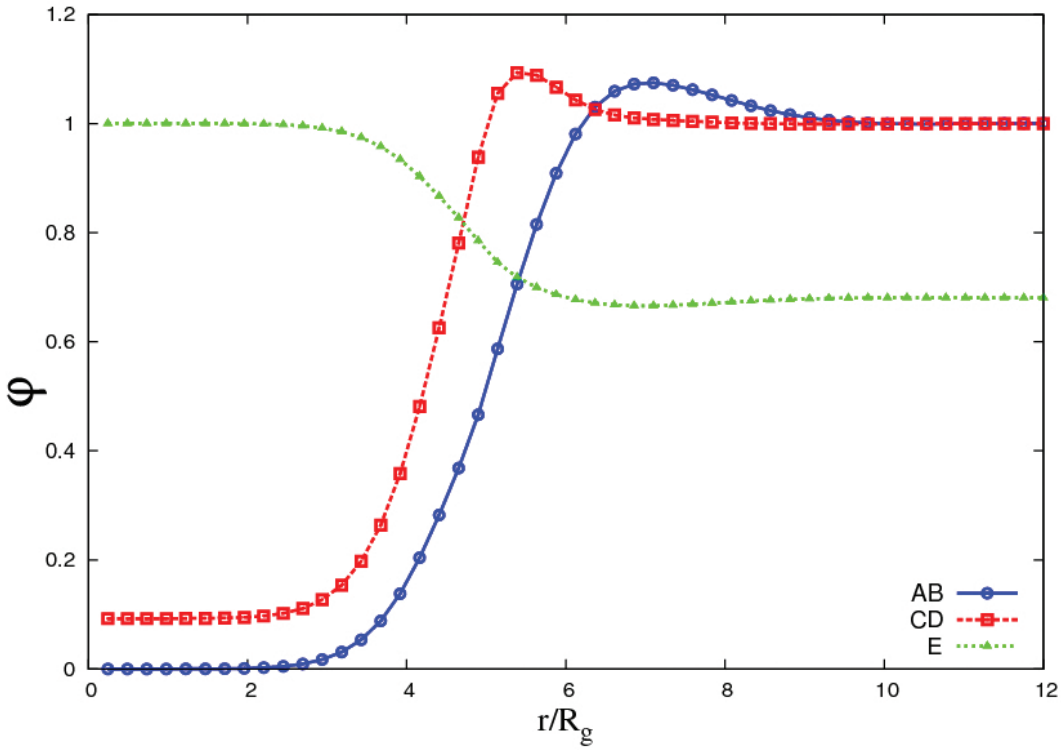

Figure 5.6: Total concentration of each polymer species as a function of the radial direction. The increase in the CD concentration quantifies the amount of separation in the system.

accommodate the geometric constraints, for example around proteins, could be one application of highly diverse lipid bilayers.

Chapter 6

Summary

In the work presented, the SCFT was used to study the mechanical properties of bilayer membranes by modelling the lipids as diblock copolymers. The mechanical properties explored were the bending modulus κ_M, Gaussian bending modulus κ_G, as well as higher order moduli denoted as the cylindrical, and spherical fourth-order bending moduli B_C and B_S, respectively. Another property calculated was the edge line tension of a bilayer pore (γ_L). All of the above parameters play an important role in the mechanical strength, morphology and function of lipid bilayers, therefore accurate calculation and understanding of the underlying physics is important. The first system modelled the lipid bilayer as a mixture of AB diblock copolymers and C homopolymers. The interaction parameters were set to allow for the AB diblocks to act as the amphiphilic phospholipids, while the homopolymers modelled the solvents. The geometry of the system was modified to measure the energy penalty of curving a cylindrical and spherical closed bilayer membrane. The results show that the length fraction of the head chains (f_A) had little effect on the bending modulus κ_M of the membrane, however the Gaussian bending modulus κ_G had a zero crossing transition

at $f_A \approx 0.4$, which can lead to topologically unstable systems. An increase in the interaction parameter (χN) between the hydrophobic and hydrophilic regions saw an increase in both κ_M and the magnitude of κ_G.

The effect of solvent in the system was also analyzed. By making the hydrophilic head groups and the homopolymer solvent slightly immiscible, a dramatic variation in the membrane moduli occurred. As the interaction increased, a large reduction in κ_M was found. The Gaussian bending modulus κ_G also saw a large increase with the interaction parameter. For relatively small changes to the solvent conditions, κ_G takes on globally positive values, which means that the spherical topology is much less stable. Another solvent parameter explored was the homopolymer length fraction κ. When the homopolymer took on larger lengths than the diblock, it was less able to hydrate the bilayer, which reduced the bending modulus of the system. This is a similar consequence as an increase in the solvent interaction. The Gaussian bending modulus κ_G also saw an increase with the homopolymer length fraction κ, although not as dramatic as with the interaction case. These results show that the solvent environment plays a large role in the membrane properties, and should be the focus of future research.

The moduli were calculated by comparing the free energy as a function of curvature to the Helfrich model. The Helfrich model is known to be accurate for low curvature systems, however an understanding of the model's limitations for high curvature has not been extensively studied. To addressed this, the SCFT was used to calculate the bending energy for bilayers that have a curvature on the order of the bilayer thickness d. In this regime, fourth-order energy terms enter the Helfrich model, and these moduli were calculated. This was done for an AB diblock, A homopolymer blend,

and the fourth-order moduli were calculated for various hydrophilic chain fractions f_A and interaction parameters χN. The results found non-zero values of these bending moduli, showing that higher order terms are non-negligible at high curvature in simple bilayer systems. Depending on the system parameters, the importance of these terms was studied. By defining a criteria for the accuracy as the relative energy difference between the Helfrich and high-order model, a critical curvature phase diagram was created. This phase diagram shows that at low curvature, the Helfrich model is an accurate representation of the bending energetics of the system, however for regions of high curvature, the fourth-order moduli become important and must be used for proper calculation. These conclusions show that in most cases, the Helfrich free energy can successfully model the bending energy of the system, and therefore validates its usage in the current literature. However, for systems exhibiting extreme curvature, as is found in certain cellular processes, the higher order model must be used.

The next set of studies focused on the effect of mixing two different types of diblock copolymers in the bilayer membrane. In biological systems, there is a large variability in the kinds of lipids present in various membrane bound systems, such as the organelles in the cell. This work focused on the mixing of variable lipid geometries and their effect on the bending modulus of the system. In this study, the secondary diblock (CD) was set to have the same chemistry as the primary diblock (AB), with the same head length ($f_A = \kappa_1 f_C = 0.5$), however a reduced hydrophobic core. The bending modulus κ_M was calculated for different relative diblock compositions (Ψ). The rigidity was calculated for different conical shapes of the secondary diblock. The bending modulus κ_M shows a nearly linear transition from one diblock type to the other. These results are similar to the work of Szleifer *et al.* [15] for the free exchange

model.

The last set of calculations focused on understanding the effect that mixing dibocks has on the edge line tension of membrane pores. The same two-component bilayers were used, and the edge line tension of the system was calculated using the SCFT. For conical secondary diblocks (CD), a large drop in line tension was found as the concentration of CD increased. In cases of very short tail length ($f_D < 0.3$), mixtures were able to reduce the line tension to negative values, which means that these systems can have a stabilizing effect on membrane pores and can be used as edge stabilization agents. Interestingly, upon addition of the conical diblocks, phase separation of these secondary blocks at the pore edge occurred. This is because the cone geometry is more suited to high positive curvature regions. These results may shed light on the reasons why high variability of lipids in biological membranes are present.

This thesis has given a systematic method to study the bilayer membrane using SCFT and has proven to be a novel approach to studying these interesting and complex systems. The framework developed can be easily extended and modified to study many other systems such as charged polymers, protein system and systems of more complex chain topologies. Since many industrial, medical and biological system have use for bilayer membranes, this research has wide potential applications.

Appendix A

Numerical Methods

The majority of the numerical cost of the SCFT comes from the calculation of the propagators, and the many iterations for needed convergence of the fields. Each step involves finding the solutions of the modified diffusion equations along the chain contour in order to calculate the propagators. The propagators are used to determine the fields and free energy of the system. The fields are updated self-consistently until a saddle point solution is reached. In many cases, this can be done using a spectral method if the final structure is known a priori and a suitable number of basis functions can be used in the calculation. In the cases where the outcome profile is not known, as such in the case of finding new morphologies, a real space method is commonly chosen [34]. The problem becomes more complicated in non-planar geometries, as the diffusion operator takes a different form in cylindrical and spherical coordinates. While having a planar geometry allows for the use of a variety of real space and pseudo-spectral (collocation) methods, the use of these different coordinate systems causes the numerics to be more complex.

For one-dimensional systems, the modified diffusion equation can be solved by finite difference methods using a Crank-Nicolson scheme [47], however in two-dimensions and higher, this becomes numerically intractable. For two-dimensional systems, the alternating direction implicit method (ADI) is used in order to solve the diffusion equations in two dimensions. A description of the Crank-Nicolson method in all three geometries considered (planar, cylindrical and spherical) will first be given, which will create a general framework for the ADI method description in cylindrical coordinates.

A.1 Crank-Nicolson Method

The Crank-Nicolson method [47] is a finite difference scheme, originally used to solve heat diffusion systems. It consists of using a simple trapezoidal rule in the time domain, and a weighted central difference for the spatial coordinate. This is the method used to solve the modified diffusion equations,

$$\frac{\partial q(\mathbf{r}, s)}{\partial s} = C\nabla^2 q(\mathbf{r}, s) - \omega(\mathbf{r}) q(\mathbf{r}, s) \tag{A.1}$$

where the coordinate system and dimension will be subject to change.

The first and simplest geometry described is the planar case. With this shown, the major highlights and changes needed to accommodate the cylindrical and spherical geometries will be discussed.

A.1.1 Planar Coordinate System

In the planar coordinate system, the Laplace operator reduces to,

$$\nabla^2 = \frac{\partial^2}{\partial x^2} \tag{A.2}$$

which greatly simplifies the problem. The Crank-Nicolson method is a combination of time-step and spatial averaging which is represented as,

$$\frac{q_i^{s+1} - q_i^s}{\Delta s} = C[\mathcal{C}_{NK}^2(q_i^{s+1})] - \frac{w_i}{2}(q_i^{s+1} + q_i^s) \tag{A.3}$$

where the spatial coordinate is indexed on a discrete grid by the subscript i, and $\mathcal{C}_{NK}^2(q_i^{s+1})$ represents a second-order central difference equation given as,

$$\mathcal{C}_{NK}^2(q_i^{s+1}) = \frac{1}{2(\Delta x)^2}(q_{i+1}^{s+1} - 2q_i^{s+1} + q_{i-1}^{s+1} + q_{i+1}^s - 2q_i^s + q_{i-1}^s) \tag{A.4}$$

This definition can be applied to the above equations. Isolating terms of the same time-step (s or $s+1$) to separate sides yields,

$$\begin{aligned} &\frac{-C\Delta s}{2\Delta x^2} q_{i+1}^{s+1} + \left(1 + \frac{C\Delta s}{\Delta x^2} + \frac{\Delta s \omega_i}{2}\right) q_i^{s+1} - \frac{C\Delta s}{2\Delta x^2} q_{i-1}^{s+1} \\ &= \frac{C\Delta s}{2\Delta x^2} q_{i+1}^s + \left(1 - \frac{C\Delta s}{\Delta x^2} - \frac{\Delta s \omega_i}{2}\right) q_i^s + \frac{C\Delta s}{2\Delta x^2} q_{i-1}^s \end{aligned} \tag{A.5}$$

Simplification is done by using scalar constants in the equation as,

$$\begin{aligned} &\alpha q_{i+1}^{s+1} + \beta q_i^{s+1} + \alpha q_{i-1}^{s+1} \\ &= -\alpha q_{i+1}^s + \gamma q_i^s - \alpha q_{i-1}^s \end{aligned} \tag{A.6}$$

where the constants are defined as,

$$\alpha = \frac{-C\Delta s}{2\Delta x^2} \tag{A.7a}$$

$$\beta = \left(1 + \frac{C\Delta s}{\Delta x^2} + \frac{\Delta s \omega_i}{2}\right) \tag{A.7b}$$

$$\gamma = \left(1 - \frac{C\Delta s}{\Delta x^2} - \frac{\Delta s \omega_i}{2}\right) \tag{A.7c}$$

This can now be put into a matrix form and then solved using a tridiagonal matrix algorithm (Thomas Algorithm/TDMA), however this step will be left for the more complicated case of a two-dimensional system, as the same methods apply in a more general scope. The same description can be applied to the cylindrical and spherical geometries.

A.1.2 Cylindrical Coordinate System

The one-dimensional Laplace operator in the cylindrical coordinates can be defined in a similar way to the planar, however since axial (z-coordinate) and angular symmetry are assumed, only the radial component of the operator is defined,

$$\nabla^2 = \frac{\partial^2}{\partial r^2} + \frac{1}{r}\frac{\partial}{\partial r} \tag{A.8}$$

As above, the differential equation can be written as,

$$\frac{q_i^{s+1} - q_i^s}{\Delta s} = C[\mathcal{C}_{NK}^2(q_i^{s+1}) + \frac{1}{r}\mathcal{C}_{NK}(q_i^{s+1})] - \frac{\omega_i}{2}(q_i^{s+1} + q_i^s) \tag{A.9}$$

where once again $\mathcal{C}_{NK}^2(q_i^{s+1})$ is defined as in Eqn. A.4, $\mathcal{C}_{NK}(q_i^{s+1})$ and r are defined as,

$$\mathcal{C}_{NK}(q_i^{s+1}) = \frac{1}{4\Delta r}(q_{i+1}^{s+1} - q_{i-1}^{s+1} + q_{i+1}^{s} - q_{i-1}^{s}) \tag{A.10}$$

$$r = r_0 + i\Delta r \tag{A.11}$$

where r_0 is the distance from the centre of the geometry to the innermost edge of the computation cell, and r is defined as the radial position within the boundaries of the cell. By separating the contour steps, a set of equations is found that can easily be placed into matrix form and solved using the TDMA. The equations in this case are slightly modified from that of the planar geometry and is given as,

$$\begin{aligned}\left(-\frac{C\Delta s}{2\Delta r^2} - \frac{1}{r}\frac{C\Delta s}{4\Delta r}\right) q_{i+1}^{s+1} + \left(1 + \frac{\Delta s}{2}\omega_i + \frac{C\Delta s}{\Delta r^2}\right) q_i^{s+1} + \left(-\frac{C\Delta s}{2\Delta r^2} + \frac{1}{r}\frac{C\Delta s}{4\Delta r}\right) q_{i-1}^{s+1} \\ = \left(+\frac{C\Delta s}{2\Delta r^2} + \frac{1}{r}\frac{C\Delta s}{4\Delta r}\right) q_{i+1}^{s} + \left(1 - \frac{\Delta s}{2}\omega_i - \frac{C\Delta s}{\Delta r^2}\right) q_i^{s} + \left(\frac{C\Delta s}{2\Delta r^2} - \frac{1}{r}\frac{C\Delta s}{4\Delta r}\right) q_{i-1}^{s}\end{aligned}$$

A.1.3 Spherical Coordinate System

The spherical Laplace operator in the case of spherical symmetry is defined as,

$$\nabla^2 = \frac{\partial^2}{\partial r^2} + \frac{2}{r}\frac{\partial}{\partial r} \tag{A.12}$$

When a comparison is made between the cylindrical and spherical Laplace operator it is clear that the only difference is that the first order derivatives are multiplied by a factor of 2. Using the same methods as in the planar and cylindrical systems, the system of equations for the spherical geometry become,

$$\left(-\frac{C\Delta s}{2\Delta r^2}-\frac{1}{r}\frac{C\Delta s}{2\Delta r}\right)q_{i+1}^{s+1}+\left(1+\frac{\Delta s}{2}\omega_i+\frac{C\Delta s}{\Delta r^2}\right)q_i^{s+1}+\left(-\frac{C\Delta s}{2\Delta r^2}+\frac{1}{r}\frac{C\Delta s}{2\Delta r}\right)q_{i-1}^{s+1}$$
$$=\left(+\frac{C\Delta s}{2\Delta r^2}+\frac{1}{r}\frac{C\Delta s}{2\Delta r}\right)q_{i+1}^{s}+\left(1-\frac{\Delta s}{2}\omega_i-\frac{C\Delta s}{\Delta r^2}\right)q_i^{s}+\left(\frac{C\Delta s}{2\Delta r^2}-\frac{1}{r}\frac{C\Delta s}{2\Delta r}\right)q_{i-1}^{s}$$

A.1.4 Crank-Nicolson Boundary Conditions

In the previous sections, a system of equations was derived to solve the diffusion equations, which can easily be represented in matrix form. As mentioned, this process will be described in detail in the following section describing the alternating direction implicit method (ADI) method. As a preamble, the effect of different boundary conditions in the Crank-Nicolson method is discussed. For this purpose, the focus will be on the planar geometry, as it is the simplest to write and understand, however the method is easily applied to the cylindrical and spherical systems with small modifications of the variable definitions.

The first step is to represent Eq. A.7 in a matrix form. The matrix will be in tridiagonal form, however at the bounding points for $i = 0$ and $i = N_x$, a value must be determined for the propagators corresponding to q_{-1} and q_{N_x+1}, respectively. How to define these points is the core to the boundary condition question. In the following, the three most common types of boundary conditions are discussed, and a simplified matrix representation of the system of equations will be shown.

Periodic Boundary Conditions

While the periodic boundary condition (PBC) is not used in the work presented, it may prove useful to the curious reader. In general, the PBC is used to represent

systems that are infinite in space or are expected to have some underlying periodicity. In molecular dynamics (MD) simulations, this is used to simulate an infinite bilayer system and evaluate the fluctuation spectra to extract bilayer properties such as the bending modulus κ_M [9,38]. In the context of the SCFT, the PBC assumes that the form of the solution to the system of equations has some periodicity. How this relates to the values of the propagators is as follows,

$$q_{-1} = q_{N_x} \tag{A.13}$$

$$q_{Nx+1} = q_0 \tag{A.14}$$

where the first equation is for the lower boundary and the second for the upper. With this in mind, the system of equations can be written in matrix form for the given set of boundary conditions as,

$$\begin{bmatrix} \beta & -\alpha & 0 & \cdots & -\alpha \\ -\alpha & \beta & -\alpha & \cdots & 0 \\ \vdots & \ddots & \ddots & \ddots & \vdots \\ 0 & \cdots & -\alpha & \beta & -\alpha \\ -\alpha & \cdots & 0 & -\alpha & \beta \end{bmatrix} \begin{bmatrix} q_0^{s+1} \\ q_1^{s+1} \\ \vdots \\ q_{N_x-1}^{s+1} \\ q_{N_x}^{s+1} \end{bmatrix} = \begin{bmatrix} \gamma & \alpha & 0 & \cdots & \alpha \\ \alpha & \gamma & \alpha & \cdots & 0 \\ \vdots & \ddots & \ddots & \ddots & \vdots \\ 0 & \cdots & \alpha & \gamma & \alpha \\ \alpha & \cdots & 0 & \alpha & \gamma \end{bmatrix} \begin{bmatrix} q_0^{s} \\ q_1^{s} \\ \vdots \\ q_{N_x-1}^{s} \\ q_{N_x}^{s} \end{bmatrix}$$

The system of equations is in tridiagonal form with the exception of the first and last equations where the periodic conditions take place. In this situation, efficient methods of finding the solution, such as the TDMA, can be used with slight modification. The TDMA method can be used in all interior points, however separate

solutions for the boundaries must be put in by hand before application of the method.

Dirichlet Boundary Conditions (Fixed Point BC)

The next common set of boundary conditions is the Dirichlet, or fixed point boundary condition. For example, when solving the heat equation across some region where one side is held constant due to contact with a heat reservoir, one may apply this boundary condition so that the solution is fixed at that point. In terms of the propagators,

$$q_0 = a \tag{A.15}$$

$$q_{N_x} = b \tag{A.16}$$

This means that the exact value of the first and last equation at all contour steps are known. This manifests itself in matrix form as,

$$\begin{bmatrix} 1 & 0 & 0 & \cdots & 0 \\ -\alpha & \beta & -\alpha & \cdots & 0 \\ \vdots & \ddots & \ddots & \ddots & \vdots \\ 0 & \cdots & -\alpha & \beta & -\alpha \\ 0 & \cdots & 0 & 0 & 1 \end{bmatrix} \begin{bmatrix} a \\ q_1^{s+1} \\ \vdots \\ q_{N_x-1}^{s+1} \\ b \end{bmatrix} = \begin{bmatrix} 1 & 0 & 0 & \cdots & 0 \\ \alpha & \gamma & \alpha & \cdots & 0 \\ \vdots & \ddots & \ddots & \ddots & \vdots \\ 0 & \cdots & \alpha & \gamma & \alpha \\ 0 & \cdots & 0 & 0 & 1 \end{bmatrix} \begin{bmatrix} a \\ q_1^{s} \\ \vdots \\ q_{N_x-1}^{s} \\ b \end{bmatrix}$$

Neumann Boundary Conditions (Zero-Derivative BC)

The final boundary condition to discuss has been exclusively used in the work presented. The Neumann boundary conditions, also referred to as the zero-derivative, or

zero-flux condition, is used when it is assumed that at the boundary, the change (or slope) of the solution is zero. In this framework, it can be thought that the values of the solutions at the boundary are extended and maintained at whatever constant value it has admitted. The form of this condition is given as,

$$\frac{\partial q_0}{\partial x} = \frac{\partial q_{N_x}}{\partial x} = 0 \tag{A.17}$$

Focusing on one of these conditions, the first order derivative in a central difference scheme gives,

$$\frac{\partial q_0}{\partial x} = \frac{q_1 - q_{-1}}{2\Delta x} = 0 \tag{A.18}$$

which leads to the conclusion that $q_{-1} = q_1$. The same calculation for the upper boundary gives $q_{Nx+1} = q_{Nx-1}$. Writing in matrix form,

$$\begin{bmatrix} \beta & -2\alpha & 0 & \cdots & 0 \\ -\alpha & \beta & -\alpha & \cdots & 0 \\ \vdots & \ddots & \ddots & \ddots & \vdots \\ 0 & \cdots & -\alpha & \beta & -\alpha \\ 0 & \cdots & 0 & -2\alpha & \beta \end{bmatrix} \begin{bmatrix} q_0^{s+1} \\ q_1^{s+1} \\ \vdots \\ q_{N_x-1}^{s+1} \\ q_{N_x}^{s+1} \end{bmatrix} = \begin{bmatrix} \gamma & 2\alpha & 0 & \cdots & 0 \\ \alpha & \gamma & \alpha & \cdots & 0 \\ \vdots & \ddots & \ddots & \ddots & \vdots \\ 0 & \cdots & \alpha & \gamma & \alpha \\ 0 & \cdots & 0 & 2\alpha & \gamma \end{bmatrix} \begin{bmatrix} q_0^{s} \\ q_1^{s} \\ \vdots \\ q_{N_x-1}^{s} \\ q_{N_x}^{s} \end{bmatrix}$$

Both the Dirichlet and Neumann conditions can use the TDMA without any modification to the standard method.

A.2 Alternating Direction Implicit Method (ADI) In Cylindrical Coordinates

The alternating direction implicit (ADI) method was first developed by Peaceman and Rachford [48] to solve the two-dimensional head diffusion equation. The ADI method is a type of operator splitting method that works by first solving a system of equations along one dimension, and then using these intermediate solutions as the initial conditions for solving the second dimension. In this work, this method is used to solve the modified diffusion equations of the chain propagators in the cylindrical geometry. As a reminder, the modified diffusion equation is,

$$\frac{\partial q(\mathbf{r}, s)}{\partial s} = C\nabla^2 q(\mathbf{r}, s) - \omega(\mathbf{r}) q(\mathbf{r}, s) \tag{A.19}$$

where $q(\mathbf{r}, s)$ is the chain propagator that depends on the positions defined by $\mathbf{r}$ and the chain segment number s. C is the diffusion coefficient, which in the case of polymeric systems is given as R_g^2, however for this work, the system has been scaled such that $R_g = 1$ and therefore $C = 1$. The $\omega(\mathbf{r})$ term is the auxiliary field that mediates the interactions between the polymers. This term is a modification of the standard diffusion case and must be treated with care. The initial condition for this system is,

$$q(\mathbf{r}, 0) = 1.0 \tag{A.20}$$

At this point, a definition of the Laplacian operator must be determined. In the next two subsections, a description of the two coordinate systems used (planar

and cylindrical) is given and a system of equations is derived that can be solved numerically to yield a solution to the modified diffusion equation.

In the cylindrical geometry, the Laplacian operator takes the form,

$$\nabla^2 = \frac{1}{r}\frac{\partial}{\partial r}\left(r\frac{\partial}{\partial r}\right) + \frac{\partial^2}{\partial z^2} = \frac{\partial^2}{\partial r^2} + \frac{1}{r}\frac{\partial}{\partial r} + \frac{\partial^2}{\partial z^2} \tag{A.21}$$

where angular symmetry of the cylinder is assumed. To perform the ADI method, the radial direction is solved first (explicit), while keeping the z-direction fixed (implicit). The solution of this first pass will constitute a half-step in the chain variable, taking it from $q(\mathbf{r}, s)$ to $q(\mathbf{r}, s + 1/2)$. Once this is complete, the $q(\mathbf{r}, s + 1/2)$ solutions are used as inputs to solve the z-direction while keeping the radial variables fixed. This final step will take the chain variable from $q(\mathbf{r}, s + 1/2)$ to the final $q(\mathbf{r}, s + 1)$, which is the desired result. Continuing this process from $s = 0$ to $s = N$, will give the solution.

In numerical calculations, methods are limited to a discrete number of points to represent continuous functions in both the spatial $(\mathbf{r}, z)$ and contour (s) dimensions. Therefore, a finite spatial grid denoting the radial values as the subscript i and the z-direction variables by the subscript j is used. The contour variables are placed as superscripts for clarity, so all future descriptions will represent the propagator as $q^s_{i,j}$. The first step of the method is written as,

$$\frac{q^{s+1/2}_{i,j} - q^s_{i,j}}{(\Delta s/2)} = \left(\delta_r^2 q^{s+1/2}_{i,j} + \frac{1}{r}\delta_r q^{s+1/2}_{i,j} + \delta_z^2 q^s_{i,j}\right) - \omega_{i,j}\frac{(q^{s+1/2}_{i,j} - q^s_{i,j})}{2} \tag{A.22}$$

The δ_r^2, δ_r, and δ_z^2 represent the second, and first order central difference equations

in both the radial and z-directions as formulated,

$$\delta_r^2 q_{i,j}^{s+1/2} = \frac{1}{(\Delta r)^2}(q_{i+1,j}^{s+1/2} - 2q_{i,j}^{s+1/2} + q_{i-1,j}^{s+1/2}) \tag{A.23}$$

$$\delta_r q_{i,j}^{s+1/2} = \frac{1}{2\Delta r}(q_{i+1,j}^{s+1/2} - q_{i-1,j}^{s+1/2}) \tag{A.24}$$

$$\delta_z^2 q_{i,j}^{s} = \frac{1}{(\Delta z)^2}(q_{i,j+1}^{s} - 2q_{i,j}^{s} + q_{i,j-1}^{s}) \tag{A.25}$$

The auxiliary field term $\omega_{i,j}$ is split between the time-steps $q_{i,j}^{s+1/2}$ and $q_{i,j}^{s}$, which essentially evaluates the variable at $q_{i,j}^{s+1/4}$. By substituting the above values into Eqn. A.22 and arranging all $q^{s+1/2}$ terms on the left hand side, and the q^s terms on the right hand side,

$$\alpha_1 q_{i+1,j}^{s+1/2} + \alpha_0 q_{i,j}^{s+1/2} + \alpha_{-1} q_{i-1,j}^{s+1/2} = \beta_1 q_{i,j+1}^{s} + \beta_0 q_{i,j}^{s} + \beta_{-1} q_{i,j-1}^{s} \tag{A.26}$$

where the left side variables are defined as,

$$\alpha_1 \equiv -\frac{C\Delta s}{2(\Delta r)^2} - \frac{1}{r}\frac{C\Delta s}{4\Delta r} \tag{A.27a}$$

$$\alpha_0 \equiv 1 + \frac{C\Delta s}{(\Delta r)^2} + \frac{\Delta s}{4}\omega_{i,j} \tag{A.27b}$$

$$\alpha_{-1} \equiv -\frac{C\Delta s}{2(\Delta r)^2} + \frac{1}{r}\frac{C\Delta s}{4\Delta r} \tag{A.27c}$$

and the right hand side variables are defined as,

$$\beta_1 \equiv \frac{C\Delta s}{2(\Delta z)^2} \tag{A.28a}$$

$$\beta_0 \equiv 1 - \frac{C\Delta s}{(\Delta z)^2} - \frac{\Delta s}{4}\omega_{i,j} \tag{A.28b}$$

$$\beta_{-1} \equiv \frac{C\Delta s}{2(\Delta z)^2} \tag{A.28c}$$

The zero-derivative (Neumann) boundary conditions is used at $i = 0, N_r$ and $j = 0, N_z$, where N_r and N_z are the upper indices for the radial and z-coordinate directions, respectively. The mathematical form of the boundary conditions is,

$$\frac{\partial q_{0,j}}{\partial r} = \frac{\partial q_{N_r,j}}{\partial r} = \frac{\partial q_{i,0}}{\partial z} = \frac{\partial q_{i,N_z}}{\partial z} = 0 \tag{A.29}$$

Taking $q_{0,j}$ as an example, the derivative is represented by the central difference method,

$$\frac{\partial q_{0,j}}{\partial r} = \frac{q_{1,j} - q_{-1,j}}{2\Delta r} = 0 \tag{A.30}$$

which leads to $q_{-1,j} = q_{1,j}$.

In this example, for $i = 0$, the system of equations at this boundary become,

$$(\alpha_1 + \alpha_{-1})q_{1,j}^{s+1/2} + \alpha_0 q_{0,j}^{s+1/2} = \beta_1 q_{0,j+1}^{s} + \beta_0 q_{0,j}^{s} + \beta_{-1} q_{0,j-1}^{s} \tag{A.31}$$

where the boundary has been enforced on the left side of the equation. The last consideration is the case where the boundary conditions must be applied in both directions, which makes up the four corners of the computation cell. As an example,

the system of equations when $i = j = 0$ is,

$$(\alpha_1 + \alpha_{-1})q_{1,0}^{s+1/2} + \alpha_0 q_{0,0}^{s+1/2} = (\beta_1 + \beta_{-1})q_{0,1}^{s} + \beta_0 q_{0,0}^{s} \tag{A.32}$$

Now that all boundary conditions have been properly considered, the system is expressed in matrix form. For the system of equations at the boundary $i = j = 0$,

$$\begin{bmatrix} \alpha_0 & (\alpha_1 + \alpha_{-1}) & 0 & \cdots & 0 \\ \alpha_{-1} & \alpha_0 & \alpha_1 & \cdots & 0 \\ \vdots & \ddots & \ddots & \ddots & \vdots \\ 0 & \cdots & \alpha_{-1} & \alpha_0 & \alpha_1 \\ 0 & \cdots & 0 & (\alpha_1 + \alpha_{-1}) & \alpha_0 \end{bmatrix} \begin{bmatrix} q_{0,0}^{s+1/2} \\ q_{1,0}^{s+1/2} \\ \vdots \\ q_{N_r-1,0}^{s+1/2} \\ q_{N_r,0}^{s+1/2} \end{bmatrix} = \begin{bmatrix} (\beta_1 + \beta_{-1})q_{0,1}^{s} + \beta_0 q_{0,0}^{s} \\ (\beta_1 + \beta_{-1})q_{1,1}^{s} + \beta_0 q_{1,0}^{s} \\ \vdots \\ (\beta_1 + \beta_{-1})q_{N_r-1,1}^{s} + \beta_0 q_{N_r-1,0}^{s} \\ (\beta_1 + \beta_{-1})q_{N_r,1}^{s} + \beta_0 q_{N_r,0}^{s} \end{bmatrix}$$

For all the interior points $j = 1, N_z - 1$,

$$\begin{bmatrix} \alpha_0 & (\alpha_1 + \alpha_{-1}) & 0 & \cdots & 0 \\ \alpha_{-1} & \alpha_0 & \alpha_1 & \cdots & 0 \\ \vdots & \ddots & \ddots & \ddots & \vdots \\ 0 & \cdots & \alpha_{-1} & \alpha_0 & \alpha_1 \\ 0 & \cdots & 0 & (\alpha_1 + \alpha_{-1}) & \alpha_0 \end{bmatrix} \begin{bmatrix} q_{0,0}^{s+1/2} \\ q_{1,0}^{s+1/2} \\ \vdots \\ q_{N_r-1,0}^{s+1/2} \\ q_{N_r,0}^{s+1/2} \end{bmatrix} = \begin{bmatrix} \beta_1 q_{0,j+1}^{s} + \beta_0 q_{0,j}^{s} + \beta_{-1} q_{0,j-1}^{s} \\ \beta_1 q_{1,j+1}^{s} + \beta_0 q_{1,j}^{s} + \beta_{-1} q_{1,j-1}^{s} \\ \vdots \\ \beta_1 q_{N_r-1,j+1}^{s} + \beta_0 q_{N_r-1,j}^{s} + \beta_{-1} q_{N_r-1,j-1}^{s} \\ \beta_1 q_{N_r,j+1}^{s} + \beta_0 q_{N_r,j}^{s} + \beta_{-1} q_{N_r,j-1}^{s} \end{bmatrix}$$

The system of equations can be solved using the tridiagonal matrix algorithm (TDMA) [49, 50], where the TDMA is a combination of back substitution and Gaussian elimination.

The solutions ($q^{s+1/2}$) are used as the initial conditions for the second step of the

ADI method. The derivation for this is the same as above,

$$\gamma_1 q_{i,j+1}^{s+1} + \gamma_0 q_{i,j}^{s+1} + \gamma_{-1} q_{i,j-1}^{s+1} = \sigma_1 q_{i+1,j}^{s+1/2} + \sigma_0 q_{i,j}^{s+1/2} + \sigma_{-1} q_{i-1,j}^{s+1/2} \tag{A.33}$$

with the constants on the left hand side matrix,

$$\gamma_1 = -\frac{C\Delta s}{2(\Delta z)^2} \tag{A.34a}$$

$$\gamma_0 = 1 + \frac{C\Delta s}{(\Delta z)^2} + \frac{\Delta s}{4}\omega_{i,j} \tag{A.34b}$$

$$\gamma_{-1} = -\frac{C\Delta s}{2(\Delta z)^2} \tag{A.34c}$$

and right hand side,

$$\sigma_1 = \frac{C\Delta s}{2(\Delta r)^2} + \frac{1}{r}\frac{C\Delta s}{4\Delta r} \tag{A.35a}$$

$$\sigma_0 = 1 - \frac{C\Delta s}{(\Delta r)^2} - \frac{\Delta s}{4}\omega_{i,j} \tag{A.35b}$$

$$\sigma_{-1} = \frac{C\Delta s}{2(\Delta r)^2} - \frac{1}{r}\frac{C\Delta s}{4\Delta r} \tag{A.35c}$$

With a final application of the TDMA, the solutions are propagated from s to $s+1$. Performing the same calculations for $s = 0, N_s$, where N_s is the number of segments, leads to the final solutions. With the chain propagators determined, the concentration and free energies can now be calculated.

Bibliography

[1] A.F. Bitbol, D. Constantin, and J.B. Fournier. *PloS one*, 7(11):e48306, 2012.

[2] B.J. Reynwar, G. Illya, V.A. Harmandaris, M.M. Müller, K. Kremer, and M. Deserno. *Nature*, 447(7143):461–464, 2007.

[3] K. Katsov, M. Müller, and M. Schick. *Biophys. J.*, 87(5):3277–3290, 2004.

[4] J. Yoo, M.B. Jackson, and Q. Cui. *Biophys. J.*, 104(4):841–52, 2013.

[5] Y. Oya and T. Kawakatsu. *Adv. Nat. Sci.: Nanosci. Nanotechnol.*, 4(1):015010, 2013.

[6] H. Lodish, A. Berk, and L.S. Zipursky. *Molecular Cell Biology*. Scientific American Books, New York, 4 edition, 2004.

[7] O.G. Mouritsen. *Life - As a matter of fat*. Springer, New York, 2005.

[8] M. Ashrafuzzaman and J. Tuszynski. *Membrane Biophysics*. Springer, New York, 2012.

[9] V.A. Harmandaris and M. Deserno. *J. Chem. Phys.*, 125(20):204905, 2006.

[10] M. Hu, J.J. Briguglio, and M. Deserno. *Biophys. J.*, 102(6):1403–1410, 2012.

[11] A. Imparato, J.C. Shillcock, and R. Lipowsky. *EPL*, 69(4):650–656, 2005.

[12] D. Marsh. *Chem. Phys. Lipids*, 144(2):146–159, 2006.

[13] T. Ohta and M. Nonomura. *EPL B*, 2(1):57–68, 1998.

[14] S.M. Oversteegen and F.A. Leermakers. *Phys. Rev. E*, 62(6):8453–8461, 2000.

[15] I. Szleifer, D. Kramer, A. Ben-Shaul, W.M. Gelbart, and S.A. Safran. *J. Chem. Phys.*, 92(11):6800, 1990.

[16] E.L. Elson, E. Fried, J.E. Dolbow, and G.M. Genin. *Annu. Rev. Biophys.*, 39:207–226, 2010.

[17] G. Illya, R. Lipowsky, and J.C. Shillcock. *J. Chem. Phys.*, 125(11):114710, 2006.

[18] R.L. Knorr, R. Dimova, and R. Lipowsky. *PloS one*, 7(3):e32753, 2012.

[19] P.B. Canham. *J THEOR BIOL*, 26(1):61–81, 1970.

[20] W. Helfrich. *Z Naturforsch C.*, 28:693–703, 1973.

[21] F.C. Frank. *Discussions of the Faraday Society*, 25:19–28, 1958.

[22] A. Pressley. *Elementary Differential Geometry*. Spinger, Great Britain, 2001.

[23] Jianfeng Li, Hongdong Zhang, Feng Qiu, and An-Chang Shi. *Phys. Rev. E*, 88:012719, 2013.

[24] J.F. Nagle. *Faraday Discussions*, 161:11, 2013.

[25] O.V. Manyuhina and J.J. Hetzel. *EPL*, 32(3):223–228, 2010.

[26] M.I. Katsnelson and A. Fasolino. *The Journal of Physical Chemistry B*, 1(1):2–7, 2006.

[27] O.V. Manyuhina and I.O. Shklyarevskiy. *Phys. Rev. Lett.*, 98:146101, 2007.

[28] S.F. Edwards. *Proc. Phys. Soc.*, 85:613, 1965.

[29] G. Zhang, F. Qiu, H. Zhang, Y. Yang, and A-C. Shi. *Macromolecules*, 43(6):2981–2989, 2010.

[30] M.W. Matsen. *EPL E*, 36(4):9857, 2013.

[31] R. Lipowsky. *Faraday Discussions*, 161:305, 2013.

[32] Y. Sakuma, T. Taniguchi, and M. Imai. *Biophys. J.*, 99(2):472–479, 2010.

[33] Jianfeng Li, Kyle A. Pastor, An-Chang Shi, Friederike Schmid, and Jiajia Zhou. *Phys. Rev. E*, 88:012718, 2013.

[34] G.H. Fredrickson. *The Equilibrium Theory of Inhomogenous Polymers*. Oxford Science Publications, New York, 2006.

[35] A. Callan-Jones, B. Sorre, and P. Bassereau. *Cold Spring Harb Perspect Biol*, 3(2):a004648, 2011.

[36] R.J.R.W. Peters, I. Louzao, and J.C.M. van Hest. *Chem. Sci.*, 3(2):335, 2012.

[37] F.Y. Jiang, Y. Bouret, and J.T. Kindt. *Biophys. J.*, 87(1):182–192, 2004.

[38] M. Deserno. Fluid lipid membranes a primer. *cmu.edu*, pages 1–29.

[39] T. Kawakatsu. *Statistical Physics of Polymers*. Springer, Germany, 2004.

[40] K. Rasmussen and G. Kalosakas. *J. Polym. Sci. Part B Polym. Phys.*, 40(16):1777–1783, 2002.

[41] M.W. Matsen. *J. Chem. Phys.*, 110(9):4658, 1999.

[42] D.A. Hammer and D.E. Discher.

[43] G. van Meer and de A.I.P.M. Kroon. *J. Cell Sci.*, 124:5–8, 2011.

[44] M.M. Kamal, D. Mills, M. Grzybek, and J. Howard. *Proc. Natl. Acad. Sci. USA*, 106(52):22245–22250, 2009.

[45] O. Sandre, L. Moreaux, and F. Brochard-Wyart. *Proc. Natl. Acad. Sci. USA*, 96:10591–10596, 1999.

[46] A. West, K. Ma, J.L. Chung, and J.T. Kindt. *J. Phys. Chem. A (to be published)*, 2013.

[47] J. Crank and P. Nicolson. *Proc. Camb. Phil. Soc.*, 43(1):5067, 1947.

[48] D.W. Peaceman and Jr. H.H. Rachford. *SIAM*, 3:28–41, 1955.

[49] L.H. Thomas. *Watson Sci. Comput. Lab. Rept., Columbia University,New York*, 1949.

[50] G.H. Bruce, D.W. Peaceman, H.H. Rachford, and J.D. Rice. *Trans. Am. Inst. Min. Engrs (Petrol Div.)*, 198, 1953.